

1 Aircraft-engine particulate matter emissions from conventional
2 and sustainable aviation fuel combustion: comparison of
3 measurement techniques for mass, number, and size

4 Joel C. Corbin^a, Tobias Schripp^b, Bruce E. Anderson^c, Greg J.
5 Smallwood^a, Patrick LeClercq^b, Ewan C. Crosbie^{c,d}, Steven Achterberg^e,
6 Philip D. Whitefield^e, Richard C. Miake-Lye^f, Zhenhong Yu^f, Andrew
7 Freedman^f, Max Trueblood^e, David Satterfield^e, Wenyan Liu^e, Patrick
8 Oßwald^b, Claire Robinson^{c,d}, Michael A. Shook^c, Richard H. Moore^c and
9 Prem Lobo^a

10 ^a*Metrology Research Centre, National Research Council Canada, Ottawa, Ontario,
11 Canada*

12 ^b*German Aerospace Center (DLR), Institute of Combustion Technology, Stuttgart,
13 Germany*

14 ^c*NASA Langley Research Center, Hampton, Virginia, USA*

15 ^d*Science Systems and Applications, Inc., Hampton Virginia, USA*

16 ^e*Center of Excellence for Aerospace Particulate Emissions Reduction Research,
17 Missouri University of Science and Technology, Rolla, Missouri, USA*

18 ^f*Aerodyne Research, Inc., Billerica, Massachusetts, USA*

19 *Correspondence to: Joel C. Corbin (Joel.Corbin@nrc-cnrc.gc.ca) and Prem Lobo
20 (Prem.Lobo@nrc-cnrc.gc.ca)*

21 0 AMT Feature: short summary (max. 500 characters incl. spaces)
22 The combustion of sustainable aviation fuels in aircraft engines produces
23 particulate matter (PM) emissions with different properties than conventional
24 fuels due to changes in fuel composition. Consequently, the response of various
25 diagnostic instruments to PM emissions may be impacted. We found no significant
26 instrument biases in terms of particle mass, number, and size measurements for
27 conventional and sustainable aviation fuel blends despite large differences in the
28 absolute magnitude of emissions.

29 1 Abstract

30 Sustainable aviation fuels (SAFs) have different compositions compared to
31 conventional petroleum jet fuels, particularly in terms of fuel sulphur and
32 hydrocarbon content. These differences may change the amount and
33 physicochemical properties of volatile and non-volatile particulate matter (nvPM)
34 emitted by aircraft engines. In this study, we evaluate whether comparable nvPM
35 measurement techniques respond similarly to nvPM produced by three blends of
36 SAFs compared to three conventional fuels. Multiple SAF blends and conventional
37 (Jet A-1) jet fuels were combusted in a V2527-A5 engine, while an additional
38 conventional fuel (JP-8) was combusted in a CFM56-2C1 engine.

39 We evaluated nvPM mass concentration measured by three real-time
40 measurement techniques: photoacoustic spectroscopy, laser-induced
41 incandescence, and the extinction-minus-scattering technique. Various commercial
42 instruments were tested including three LII 300s, one PAX, one MSS+, and two
43 CAPS PM_{2.5} Instruments. Mass-based emission indices (EI_m) reported by these
44 techniques were similar, falling within 30% of their geometric mean for EI_m above
45 100 mg/kg_{fuel} (approximately 10 µg PM m⁻³ at the instrument), this geometric
46 mean was therefore used as a reference value. Additionally, two integrative
47 measurement techniques were evaluated: filter photometry and particle size
48 distribution (PSD) integration. The commercial instruments used were one TAP,
49 one PSAP, and two SMPSs. The TAP and PSAP were operated at 5% and 10% of
50 their nominal flow rates, respectively, to extend the life of their filters. These
51 techniques are used in specific applications, such as on-board research aircraft to

Deleted: s

53 determine PM emissions at cruise. El_m reported by the alternative techniques fell
54 within approximately 50 % of the mean aerosol-phase El_m .

55 In addition, we measured PM-number-based emission indices using PSDs and
56 condensation particle counters. The commercial instruments used included TSI
57 SMPSSs, a Cambustion DMS500, and an AVL APC, and the data also fell within
58 approximately 50 % of their geometric mean. The number-based emission indices
59 were highly sensitive to the accuracy of the sampling-line penetration functions
60 applied as corrections. In contrast, the El_m data were less sensitive to those
61 corrections since a smaller volume fraction fell within the size range where
62 corrections were substantial. A separate, dedicated experiment also showed that
63 the operating laser fluence used in the LII 300 laser-induced incandescence
64 instrument for aircraft engine nvPM measurement is adequate for a range of SAF
65 blends investigated in this study. Overall, we conclude that all tested instruments
66 are suitable for the measurement of nvPM emissions from the combustion of SAF
67 blends in aircraft engines.

68 Keywords: non-volatile particulate matter, aircraft, emissions, sustainable
69 aviation fuels, black carbon

70 2 Introduction

71 Aircraft engine particulate matter (PM) emissions are composed of non-volatile
72 (black carbon, metal ash, oxygenated functional groups) and volatile components
73 (volatile organic compounds, nitrates, sulphates) (Gagné et al., 2021; Masiol and
74 Harrison, 2014; Petzold et al., 2011). The non-volatile particulate matter (nvPM)
75 emissions are formed in the combustor, while volatile particulate matter (vPM)
76 emissions, present in the gas phase at the engine exit, condense after emission.
77 Aircraft engines emit vPM with similar or greater orders of magnitude as nvPM,
78 especially after the vapour pressure of volatile species is lowered by oxidative
79 aging (Kiliç et al., 2018) or by cooling (Beyersdorf et al., 2014). The nvPM and vPM
80 are constituents of total PM which affects air quality, health, and climate. The
81 International Civil Aviation Organization (ICAO) has developed standards and
82 recommended practices (SARPs) for measuring the mass- and number-based
83 emissions of nvPM emitted from aircraft engines with maximum rated thrust >26.7

84 kN (ICAO, 2017). Currently, SARP^s have not been established for vPM or total PM
85 (Lobo et al., 2020). The SARP^s for nvPM specify standardized sampling and
86 measurement protocols (SAE, 2013, 2018; ICAO, 2017), which have been
87 extensively evaluated and validated (Lobo et al., 2015b, 2020; Kinsey et al., 2021).
88 The nvPM regulatory limits are applicable for type certification of aircraft engines,
89 but they do not address the vPM which may have substantial environmental
90 impacts.

91
92 To reduce CO₂ emissions, mitigate environmental impacts, and make the aviation
93 sector more sustainable, a significant effort is underway to develop and deploy
94 sustainable aviation fuels (SAFs). Various feedstocks and different conversion
95 pathways can be used to produce SAFs (Hileman and Stratton, 2014), which differ
96 in chemical and physical properties compared to conventional petroleum jet fuel
97 (Vozka et al., 2019), most notably by lacking aromatic and sulfur species that are
98 precursors to nvPM and vPM emissions. New SAF candidates must undergo a
99 rigorous qualification and approval process (ASTM D4054) prior to being certified
100 under the ASTM D7566 standard specification as a blending component. Currently,
101 the ASTM D7566 standard allows SAF blend ratios of up to 50% with conventional
102 fuel for drop-in fuels (Wilson et al., 2013).

103
104 The combustion of neat SAFs and blends with conventional jet fuel has been shown
105 to result in different PM emissions characteristics as a function of engine type and
106 operating condition (Beyersdorf et al., 2014; Brem et al., 2015; Corporan et al.,
107 2011; Lobo et al., 2011, 2015a, 2016; Moore et al., 2017; Schripp et al., 2018, 2019;
108 Timko et al., 2010). In addition to changes in PM mass- and number-based
109 emissions, SAF combustion results in changes to particle size distributions (PSD)
110 (Beyersdorf et al., 2014; Cain et al., 2013; Kinsey et al., 2012; Lobo et al., 2011,
111 2015a, 2016; Schripp et al., 2018; Timko et al., 2010), chemical composition (Elser
112 et al., 2019; Kinsey et al., 2012; Timko et al., 2013; Williams et al., 2012),
113 morphology (Huang and Vander Wal, 2013; Kumal et al., 2020; Liati et al., 2019),
114 hygroscopic properties (Trueblood et al., 2018), and optical properties (Elser et al.,
115 2019).

116

117 The standardized sampling and measurement protocol for aircraft engine nvPM
118 emissions was designed and validated for engine certification tests using
119 conventional jet fuel. The SARP require that number-based nvPM emissions are
120 measured with a butanol-based condensation-nuclei counter with a 50% cut-off
121 size of, at most, 10 nm sampling in single-particle-counting mode downstream of a
122 diluter and volatile particle remover. For mass-based nvPM emissions, the
123 instrument must be insensitive to vPM and able to meet performance
124 specifications for repeatability, zero drift, linearity, limit of detection, rise time,
125 sampling interval, accuracy, and applicability. Limited information is available on
126 aircraft engine nvPM emissions characteristics measured with the standardized
127 system for different engine types burning SAFs and blends with conventional fuel
128 ([Durdina et al., 2021](#)) (Durand et al., 2021; Elser et al., 2019; Lobo et al., 2015a,
129 2016).

130
131 The standardized system components are not easily adaptable for use on aircraft
132 for measurement of cruise level nvPM emissions. Consequently, there are no
133 comparable in-flight engine-emissions data available for developing and validating
134 models that predict cruise nvPM-emissions based on engine certification data.
135 Particle size distribution measurements are also not included in the standardized
136 system, which are important for assessing the effects of fuels, operating conditions,
137 and engine technologies on the environmental impacts of PM emissions. Thus to
138 advance our understanding of aircraft engine emissions and the factors that
139 control them as well as to develop a large and consistent observational data base,
140 it is important to evaluate the relative performance of other diagnostic
141 instruments that are not prescribed in the standardized protocol but meet these
142 needs. Such instruments must be evaluated for their response to nvPM and total
143 PM emissions from aircraft engines using standardized and non-standardized
144 systems, and for measurements at the engine exit plane and downstream of the
145 engine in the near field, since these instruments are typically used with minimal
146 change to their operating parameters for a wide range of sampling conditions. Very
147 limited data are available in the literature for this purpose, and no data have yet
148 been published for SAFs.

Deleted: catalytic stripper

151 Here, we present the inter-comparison of real-time measurements of aircraft
152 engine nvPM emissions in terms of physical characteristics such as mass, number,
153 and size distributions using different diagnostic instruments and measurement
154 principles. The nvPM mass emissions were evaluated using three real-time
155 measurement techniques: photoacoustic spectroscopy, the extinction-minus-
156 scattering technique, and laser-induced incandescence (LII), and two alternative
157 measurement techniques widely used in laboratories and on-board aircraft: filter-
158 based photometry and PSD integration. We note that one of the photoacoustic
159 instruments and the LII instruments have been demonstrated to be compliant with
160 the ICAO SARPs performance specifications. The PM number-based emissions
161 were measured using a condensation particle counter. The PSD characteristics
162 measured by scanning mobility particle sizers and an electrical mobility
163 spectrometer were also compared. The nvPM and total PM emissions were
164 delineated using a thermal denuder and a catalytic stripper. We also report the
165 effect of laser fluence on the laser-induced incandescence of nvPM for SAF
166 combustion as changing carbon nanostructure is known to influence particle light
167 absorption and consequently LII signals, and hence the derived nvPM mass
168 concentration. The impact of fuel composition on PM emissions will be reported
169 separately (Schripp et al., 2022).

170 **3 Methods**

171 The observations presented in this paper were collected during the NASA/DLR-
172 Multidisciplinary Airborne Experiment (ND-MAX) / Emission and Climate Impact
173 of Alternative Fuel (ECLIF) 2 campaign that was conducted at Ramstein Air Base,
174 Ramstein-Miesenbach, Germany in January-February 2018. The campaign included
175 ground-based and in-flight measurements of emissions from the DLR Advanced
176 Technology Research Aircraft (ATRA) A320 aircraft with V2527-A5 engines
177 running on two conventional jet fuels and three blends with SAF. The main
178 objective of the ground-based measurements was to characterize the nvPM, total
179 PM, and hydrocarbon emissions as functions of engine thrust condition and fuel
180 composition. Several identical instruments were included in the in-flight sampling
181 aircraft (NASA DC-8) and ground measurement diagnostic instrument suites to
182 enable comparisons of engine emissions during ground and airborne operations,

183 and create a data set for testing cruise emission models. The NASA DC-8 aircraft
184 with CFM56-2C1 engines was also used as an emissions source to compare various
185 emissions diagnostic instruments during the ground-based measurements.

186 *3.1 Engine and fuels*

187 In the majority of this work, emissions were sampled from a single IAE
188 mixed-flow V2527-A5 starboard engine of the DLR ATRA aircraft (Airbus A320-
189 232). The engine was operated on two conventional, petroleum jet fuels, referred
190 to as REF3 and REF4, and three sustainable aviation fuel blends, referred to as
191 SAF1, SAF2, and SAF3. The abbreviations for the two conventional petroleum fuels
192 are used to avoid confusion with the previous ECLIF campaign (Schripp et al.,
193 2018).

194 A limited number of experiments were also performed with JP-8 fuel,
195 combusted in the starboard CFM56-2C1 engine (#3) of the NASA DC-8 aircraft.
196 Due to limited fuel availability, none of the other five fuels could be combusted in
197 the CFM56-2C1 engine. The properties of the six fuels are summarized in Table 1.

198 *3.2 Ambient conditions*

199 The measurements presented here were performed outdoors during winter
200 in western Germany. Detailed meteorology for each test point is given in the [Data](#)
201 [Availability section](#). The minimum, median, and maximum temperatures were
202 2.3, 2.9, 8.3 °C, respectively. Conditions were humid (>83 % humidity) and
203 sometimes rainy. Winds ranged from 0 to 15.5 km h⁻¹ and wind direction was
204 sometimes variable. The median wind direction was south-westerly, while the
205 source aircraft was oriented facing to the east. Consequently, winds blowing
206 approximately 45° angle from the right rear of the source aircraft sometimes
207 prevented the engine emissions from reaching the sampling probe at low engine
208 thrust settings.

Deleted: supplement

210 *3.3 Emissions sampling*

211 An extensive suite of aerosol and gas-phase instruments operated by the
212 members of six different institutions were deployed in two different shipping

214 containers to characterize the emissions (Table 2). The complete emission-
215 sampling setup is discussed in a companion paper Schripp et al., 2022). Briefly,
216 emissions were sampled through a probe located 43 m downstream of the
217 starboard engine of the aircraft. The probe was placed in front of a blast fence
218 located on the western side of the Ramstein Air Force Base flight line, and the fence
219 redirected the engine exhaust upwards for safety. The probe was connected to a
220 18.5-mm ID, 20-m-long electrically-conductive sampling line heated to 60 °C, that
221 transported flow to a sampling plenum maintained at 33 °C. To minimize residence
222 time and particle losses in this sampling line, a pump ensured that a total of at least
223 137 L min⁻¹ flowed through the sampling manifold at all times. Higher flows
224 produce an unacceptably large pressure drop in the primary sampling line. The
225 majority of this flow was discarded as excess.

226
227 The plenum was placed inside a modified shipping container (Container 1) behind
228 the blast fence, along with the NRC, DLR, and NASA instruments. The North
229 American Reference System (NARS) was connected to the plenum by a short
230 section of heated line to the NARS dilutor box, which was heated to 60 ± 15 °C and
231 contained a custom Dekati dilutor with a dilution factor of approximately 4 (less
232 than the standard Dekati dilutor factor of 8 to 14). A 25 m line heated to 60 ± 15 °C
233 transferred sample aerosols flow from the dilutor box to a second shipping
234 container (Container 2), where the MST and ARI instruments were connected. The
235 NARS components include the 25 m heated line, attached diluters and MST
236 instrument suite; the system is compliant with specifications for the standardized
237 nvPM sampling and measurement system (SAE, 2013; SAE, 2018; ICAO, 2017) and
238 whose performance has been demonstrated and evaluated in previous studies
239 (Lobo et al., 2015b, 2016, 2020). Additional instrumentation installed as part of
240 the NARS included a fast electrical mobility spectrometer (Cambustion DMS500),
241 an Aerodyne Aerosol Mass Spectrometer (results not presented here), and a CAPS
242 PM_{2.5} monitor (Aerodyne Research Inc.). The details of the instruments installed
243 inside these two containers are listed in Table 3.

244 3.3.1 *Gaseous measurements*

245 A suite of gaseous emissions was measured in this study, as summarized in Table
246 2. The CO₂ measurements from the NASA LI-COR 7000 were in good agreement
247 with those taken by DLR (MKS MultiGas 2030 FTIR Continuous Gas Analyzer) and
248 MST (LI-COR model 840A), but had a faster response time and were therefore used
249 as the reference for instruments in Container 1. Instruments in Container 2 used
250 the MST measurements as reference.

251 3.3.2 *nvPM number and particle size distributions (PSDs)*

252 nvPM number concentration was measured directly by a certification-test-
253 compliant, particle counter, APC (AVL Inc., which contains a TSI Model 3790E CPC
254 [and volatile particle remover](#)), which was part of the NARS in Container 2. PSDs
255 were measured with two technologies: scanning mobility particle sizers (SMPS, TSI
256 Inc.) and electrical mobility sizers (EMS). Two types of EMS were used; the
257 Cambustion DMS500 (in Container 2, measuring particles 5 to 1000 nm in
258 diameter; data processed with a bimodal calibration matrix and log-normal
259 inversion) and the TSI Engine Exhaust Particle Sizer (EEPS, Container 1, measuring
260 particles from 6 to 523 nm). However, the EEPS data were excluded from this
261 analysis due to unidentified problems with the instrument which led to anomalous
262 PSDs.

263 Two SMPSs measured nvPM PSDs. An SMPS operated by NRC measured
264 particles 10 to 278 nm in diameter downstream of a catalytic stripper (Model
265 CS015, Catalytic Instruments GmbH), which heated samples to 350 °C before
266 oxidizing gas-phase VOCs to prevent them from recondensing after exiting the
267 device. Another SMPS operated by NASA measured particles 10 to 278 nm in
268 diameter either directly or downstream of a NASA-constructed thermal denuder
269 (TD) also operated at 350 °C. The TD employs a concentric activated charcoal filter
270 downstream of the sample heater to prevent re-condensation of volatile species.
271 TDs are commonly used on-board aircraft for measuring nvPM number
272 concentration and size distributions (Clarke, 1991; Moore et al., 2017) and have
273 been shown to effectively evaporate nucleation and accumulation mode sulfate
274 and organic aerosols (Beyersdorf et al., 2014; Schrapp et al., 2018).

275 3.3.3 *nvPM mass measurements*

276 In this study, most of the nvPM mass data were derived from light
277 absorption coefficients (units of m^{-1}), either determined in flow-through sample
278 cells (the CAPS PM_{SSA}, PAX, and MSS introduced below) or after collecting particles
279 onto a filter (the TAP and PSAP introduced below). Such absorption measurements
280 can be converted to equivalent black carbon or eBC mass concentrations (eBC,
281 units of $g\ m^{-3}$; Petzold et al. (2013)) by dividing them by a reference mass
282 absorption cross-section (MAC, units of $m^2\ g^{-1}$). The LII measurements also rely on
283 light absorption, although the measurand is not absorption but incandescence at
284 two wavelengths and is termed rBC (Petzold et al., 2013; Michelsen et al., 2014).

285 The reference MAC used to report eBC represents an assumed physical
286 property of the nvPM emitted by the engine at a given time. The extensive review
287 of Bond and Bergstrom (2006) concluded that the MAC at 550 nm of externally-
288 mixed BC from a variety of sources could be summarized as $7.5 \pm 1.2\ m^2\ g^{-1}$; the
289 more recent review of in-situ measurements by (Liu et al., 2020) recommended
290 $8.0 \pm 0.7\ m^2\ g^{-1}$ at 550 nm. In this study, we have used the Bond and Bergstrom
291 value of $7.5\ m^2\ g^{-1}$ for consistency with earlier work and instrument software.
292 These values are assumed to vary inversely with wavelength, with an Angstrom
293 (power) exponent of 1; for example, the 660 nm CAPS PM_{SSA} monitor data were
294 processed with a MAC of $7.5\ m^2\ g^{-1} \times (550\ nm / 660\ nm)^1 = 6.5\ m^2\ g^{-1}$.

295 One eBC technique, the CAPS PM_{SSA} monitor (Aerodyne Research Inc.; Onasch et al.,
296 2015) derives absorption coefficients as the difference between measured aerosol
297 extinction and scattering coefficients, from which eBC concentrations were
298 calculated as described above. The CAPS PM_{SSA} measures light extinction by the
299 calibration-free cavity attenuation phase shift (CAPS) technique and light
300 scattering with an integrating nephelometer. The CAPS technique measures the
301 lifetime of photons in a high-finesse optical cavity comprised of two high
302 reflectivity mirrors, from which the extinction coefficient can be calculated. An
303 integrating nephelometer captures light scattered from a section of this cavity, and
304 is calibrated using the measured extinction of small (Rayleigh regime) non-
305 absorbing particles. In this study, two CAPS PM_{SSA} monitors were present, one
306 operated at 630 nm wavelength by ARI and the other at 660 nm wavelength by

307 NRC. The scattering channel of the NRC CAPS PM_{SSA} was calibrated on-site using
308 nebulized and dried ammonium sulfate particles; the other instruments were
309 similarly calibrated prior to the campaign at the manufacturer using 200 nm
310 ammonium sulfate. For the sub-200 nm particles measured in this study, no
311 truncation corrections (Modini et al., 2021) were necessary.

312 Two other eBC instruments were based on photoacoustic spectroscopy, namely
313 the Photoacoustic Extinctiometer (PAX, DMT Inc.; Nakayama et al., 2015) and the
314 Micro Soot Sensor (MSS; AVL GmbH; Schindler et al., 2004). In both of these
315 instruments, aerosol absorption is measured by the periodic heating of particles
316 using a modulated laser, resulting in the generation of pressure waves which are
317 amplified by an acoustic cell and detected by a microphone. The PAX was
318 calibrated using nebulized ammonium sulfate as well as graphitic nanoparticles
319 (Aquadag).

320 During on-site calibration of the PAX using graphitic Aquadag nanoparticles, the
321 PAX signals were observed to drift slowly upwards after each baseline. We were
322 nevertheless able to obtain useful data by configuring the PAX to auto-baseline
323 every 180 seconds, and only using the first 15 seconds of measurements after each
324 baseline. After the campaign, it was found that a component of the circuit board
325 was damaged during the initial shipment. In spite of this electrical problem, the
326 PAX data do not represent outliers in the following analysis.

327 Two additional pairs of eBC instruments were deployed at the ground site and on-
328 board the NASA DC-8 that measured aerosol absorption coefficients based on filter
329 attenuation, namely a Particle Soot Absorption Photometer (PSAP, Radiance
330 Research; Bond et al., 1999) and Tricolor Absorption Photometer (TAP, Brechtel
331 Manufacturing Inc.; Ogren et al., 2017). These instruments were designed as low-
332 cost, low-maintenance devices for monitoring aerosol optical properties in the
333 background atmosphere (i.e., at low concentrations) and have been used
334 previously in airborne and ground-based studies (Moore et al., 2017). In these
335 instruments, particles are continuously collected onto an internal filter while its
336 light attenuation is measured. The change in light attenuation over time is used to
337 calculate absorption coefficients. This calculation requires post-processing to

338 correct for filter loading effects (which do not require independent measurements)
339 and may also be corrected for light attenuation due to scattering rather than
340 absorption (which requires an independent nephelometer measurement)
341 (Virkkula, 2010). Other sources of error include nonlinearities due to size-
342 dependent penetration of particles into the filter media and the evaporation of
343 volatile species over time (Lack et al., 2014; Nakayama et al., 2010). We note that
344 the TAP automatically advances its filter when its transmission drops below 80%,
345 whereas the PSAP requires a manual filter change. The PSAP filter was therefore
346 changed manually before each set of experiments herein, to ensure that its filter
347 transmission remained above 80% during all measurements.

348 Three Artium LII 300 (Artium Technologies) instruments measured rBC, based on
349 two-colour pulsed laser-induced incandescence (LII) (Snelling et al., 2005). These
350 instruments heat nvPM using a 1064 nm pulsed laser and measure the resulting
351 incandescence at two wavelength bands. From this measurement, rBC temperature
352 and mass concentrations can be calculated. One of the LII 300s was a component of
353 the NARS. Of the other two, one was dedicated to an experiment where its
354 operating conditions were varied (Section 4.6). Therefore, only two LII 300s were
355 measuring real-time nvPM mass concentration simultaneously at any given time.
356 The MSS+ and the LII 300s were calibrated by reference to the elemental carbon
357 mass (defined by thermal-optical analysis) produced by a laboratory diffusion-
358 flame combustion aerosol source using measurements at three mass
359 concentrations spanning 0.1 to 0.5 mg m⁻³ (SAE, 2018).

360 Finally, the SMPS PSDs were converted to equivalent mass concentrations by the
361 integrated PSD approach, described in detail by Momenimovahed and Olfert
362 (2015). In brief, the equivalent mass of each SMPS-reported mobility diameter was
363 calculated using an effective density of 1000 kg m⁻³, which has been shown to
364 produce better than 20% accuracy relative to more complete, size-resolved
365 effective densities (Durdina et al., 2014).

366 **3.4 Data analysis**

367 **3.4.1 Emission index calculations**

368 The raw data were analysed over comparable time intervals and cross-
369 checked by independent calculations. The general analysis proceeded as described
370 in this section. First, the time series of measured CO₂ concentrations was used as a
371 reference against which to synchronize all time series, based on rapid rises and
372 falls in the observed concentrations (measured at 1 Hz) when the engine thrust
373 condition underwent large changes (as shown at 08:00 in Figure 2). All
374 instruments were synchronized against the NASA CO₂ sensor except the
375 instruments in container 2, which was synchronized against the MST LI-COR CO₂
376 sensor, because of the additional dilution stage. The time synchronization
377 accounted for different lag times due to differences in the response times and clock
378 accuracy of each instrument.

379 Second, the CO₂ concentrations [CO₂] were baseline-subtracted and filtered as
380 follows. The CO₂ baseline ([CO₂]_b) was calculated as the mean of the CO₂
381 concentrations measured before ([CO₂]₀) and after ([CO₂]₁) each test. The
382 uncertainty in this baseline value was calculated as either ([CO₂]_b – [CO₂]₀) or
383 ([CO₂]_b – [CO₂]₁), whichever was greater.

384 Due to the prevailing crosswind mentioned above, unstable CO₂ concentrations
385 occurred during some test points at the idle engine thrust condition. These
386 unstable conditions were identified and filtered using two separate methods. In
387 the first method, the SMPS PSDs were inspected for reproducibility. In the second
388 method, an algorithm was used to reject any test points with CO₂ uncertainties
389 greater than 50%, CO₂ signals less than a factor of ten greater than uncertainty, or
390 CO₂ signals less than 20% above baseline. We found that the first method rejected
391 all of the points rejected by the algorithm, in addition to a few additional points.
392 The analysis presented uses the first method.

393 Third, all data were arithmetically averaged over the test point periods defined in
394 Table S1. For each instrument, the averaging periods were refined by inspection of
395 the data since sampling-line residence times varied. The averaged data were

396 typically at 1 Hz sampling frequency initially, although the SMPS instruments
397 measured PSDs at 45 second intervals (NRC instrument) or 30 second intervals
398 (NASA). Emission indices (EIs) were then calculated from the averaged data
399 following (SAE, 2013):

$$EI_m = PM_m \frac{RT_m}{[CO_2](M_c + \alpha M_H)P_m} \quad (1)$$

400

$$EI_{num} = PN \times 10^6 \frac{RT_m}{[CO_2](M_c + \alpha M_H)P_m} \quad (2)$$

401

402 Where EI_m and EI_{num} are mass and number-based EIs, respectively; PM_m
403 and PN are mass and number concentrations, respectively, at standard reference
404 temperature (T_m ; 273.15 K) and pressure (P_m ; 1 atm); α is the hydrogen to carbon
405 ratio of the fuel; M_c and M_H are the molar masses of carbon and hydrogen,
406 respectively; and R is the ideal gas constant (0.082 L.atm.K⁻¹.mol⁻¹).

407 3.4.2 Penetration correction

408 Particles may be lost to the walls of sampling lines or to deposits on those
409 walls. The fraction of particles penetrating a given system varies with size,
410 according to a characteristic penetration function. Four penetration functions were
411 applied in this study: 1) from the probe to the sampling plenum, 2) from the
412 plenum to the NARS, 3) within the TD, and 4) within the CS (Figure 4). Function 1
413 was measured on site as described below. Function 2 was calculated using the
414 standard equations for line penetration, as detailed in the loss calculation
415 methodologies provided in SAE documents AIR6504 (SAE, 2017) and ARP6481
416 (SAE, 2019). Function 2 was adapted slightly for each instrument in the NARS due
417 to the relatively small additional losses in the sampling lines of each instrument.
418 Function 3 was experimentally determined in the laboratory by NASA. Function 4
419 was obtained from theoretical estimates and experimental measurements
420 (Catalytic Stripper manual, 2014).

421

422 Penetration function 1 (probe-to-plenum penetration) was measured
423 experimentally by nebulizing ammonium sulfate particles at the probe while all

424 instruments were sampling and all heated lines had reached thermal equilibrium.
425 (Function 1 therefore also includes the smaller instrument sampling lines
426 downstream of the plenum in its correction as well; however, these were
427 considered negligible relative to the longer probe-to-plenum and plenum-to-
428 Container-2 transport lengths.) For this measurement, the NRC SMPS was moved
429 to the probe, while the NASA instrument remained in its standard position. The
430 ratio of the NASA to NRC PSDs (GMD 30 nm, GSD 1.7) then provided a first
431 estimate of the penetration function. However, this first estimate was not accurate,
432 as the measurements were performed on a cold day (measured as approximately 5
433 °C outdoors and 15 °C in the instrument container) and as it does not account for
434 performance differences between the NASA and NRC SMPSs. Therefore, two
435 corrections were made. First, both measurements were corrected to standard
436 temperature and pressure. Second, differences between the two instruments were
437 directly measured by moving the NRC SMPS just outside of the sampling container
438 (to keep it at 5 °C) and connecting it to an identical sampling line as the NASA
439 SMPS. The ratio of the two measured PSDs in this setup was defined as equal to
440 unity at all sizes, and used to correct the initial penetration function. Therefore, no
441 further correction was made for sampling lines in Container 1. Losses in this
442 additional line were negligible (calculated penetrations of 0.997 at 100 nm and
443 0.98 at 20 nm) relative to the long NARS line to Container 2 (i.e., Function 2).

444
445 All reported data were corrected using penetration functions. Size-resolved data
446 (SMPS PSDs) were corrected using the size-resolved penetration functions shown
447 in Figure 4. Size-integrated data were corrected using either number-based (for
448 the APC) or mass-based (for all other instruments). The number-based line loss
449 corrections were calculated as the ratio of the corrected to uncorrected PSDs. The
450 mass-based corrections were calculated using the corresponding ratio of PVDs.
451 Correction factors for each test point are given in the Data Availability section.

452
453 3.5 *Uncertainties*
454 All reported uncertainties and error bars represent standard errors,
455 propagated through the calculation as necessary. When two independent sources

Deleted: are

Deleted: for

Deleted: these

Deleted: Size-integrated data (all other instruments)
Deleted: were corrected by weighting the penetration functions by
Deleted: the corresponding measured SMPS PVDs. The c

462 of uncertainty were available (for example, the standard error in the 10 second
463 averages of $[CO_2]$ and the uncertainty in the baseline value) they were added in
464 quadrature. Our bottom-up calculations of uncertainty can be compared with the
465 spread of the data points in our EI comparisons below. This spread represents a
466 top-down uncertainty, and is similar in magnitude to the bottom-up uncertainties
467 (i.e. error bars). This similarity lends confidence to our uncertainty estimates. In
468 most figures, error bars have generally been omitted for clarity, but uncertainties
469 are given for each instrument at each test point in Table S1.

470 4 Results and discussion

471 4.1 *Experiment overview*

472 A typical time series obtained when the emissions from the IAE V2527-A5 engine
473 were sampled is shown in Figure 2. Nominal low-pressure jet-engine primary fan
474 speeds ($N1$), expressed as a percentage of maximum continuous thrust, are shown
475 by the labels at the top of the figure. Percent $N1$ (along with engine fuel flow rate)
476 is another metric for representing the different engine thrust conditions and is
477 used as a primary independent variable in this study. The CO_2 concentrations (red
478 line) were highly variable at $N1 = 23\%$ as the ambient wind shifted the aircraft
479 exhaust plume toward and away from the sampling probe. Correspondingly, both
480 nvPM mass and PSD measurements were highly variable, as shown by the blue
481 trace and black symbols, respectively.

Deleted: turbine

482 As shown in Figure 3a, nvPM mass concentrations, represented by EI_m , increased
483 with increasing $N1$ before decreasing slightly at the highest $N1$, similar to the
484 trends for other engine types reported by Lobo et al. (2015b, 2020). Figure 3b
485 shows that the relationship for EI_{num} is less clear, with a slight increase at
486 moderate $N1$ followed by a greater decrease at high $N1$. As discussed below
487 (Section 4.2.3), the higher EI_m at higher $N1$ thrust was associated with larger
488 particle sizes, and therefore smaller penetration-function corrections (Section
489 4.2.1). Finally, for context, Figure 3c shows the relationship of the PM mass
490 concentrations, used to calculate EI_m (based on the geometric mean EI_m discussed
491 in Section 4.4.1), with baseline-subtracted CO_2 concentrations from the measured

494 plume. An effect of fuel composition is evident, and discussed in detail in Schripp et
495 al., (2022).

496 *4.2 Size distributions and penetration functions*

497 *4.2.1 Penetration functions*

498 A typical PSD, and corresponding PVD, are shown in Figure 4, in the context of the
499 penetration functions applied in this work. The PVD was calculated by assuming
500 spherical particles, which incurs negligible error for aircraft-engine nvPM due to
501 the small diameter of particles produced by such engines (Durdina et al., 2014;
502 Saffaripour et al., 2020). For the example PSD and PVD in Figure 4 (shading), it is
503 clear that a substantial fraction of the particle number was corrected for
504 penetrations (lines) of roughly 0.5. In contrast, the larger mode of the PVD
505 corresponds to penetrations larger than 0.8 in most cases. These differences led to
506 a median number- and mass-based correction factors of 1.51 and 1.19, respectively
507 for penetration Function 1 (probe to plenum) labelled in the figure. The remaining
508 instrument-specific penetration corrections were applied according to the position
509 of each instrument in the sampling system, as specified in Table 2. The magnitude
510 of each correction is given in Table S1.

511

512 *4.2.2 PSDs*

513 Figure 5 shows selected PSDs from the IAE V2527-A5 engine operated with SAJF1
514 (Figure 5a) and REF4 (Figure 5b) fuels. The PSDs are corrected for line penetration
515 as described above. The plot illustrates a lower (40 % N1) and a higher thrust
516 point (60 % N1) from the available data for two fuels. Note that the ordinate scales
517 are harmonized across the upper and lower rows only. All abscissa scales are
518 harmonized. The figure indicates roughly comparable PSDs from these two fuels.
519 The companion paper (Schripp et al., 2022) compares the effects of fuel
520 composition in detail.

521 The CFM56-2C1 engine on the DC-8 burning JP-8 emitted an order of magnitude
522 more total particles per unit fuel burned than any of the fuels combusted in the

523 ATRA (data not shown). We attribute this difference to the relatively high sulfur
524 content of the JP-8 fuel (1490 ppm sulfur versus ≤ 105 ppm for the other fuels).
525 The CFM56-2C1 engine also emitted a factor of three lower nvPM mass and nvPM
526 number than the V2527-A5 engine.

527 The presence of extremely small particles with $d_m < 10\text{nm}$ was evident in the two
528 nvPM PSDs (not shown due to the extremely large penetration function at these
529 sizes; Figure 4). The CS-SMPS data extended to smaller diameters, and showed that
530 the size range measured by these two instruments was insufficient to capture the
531 full PSD for the CFM56-2C1 engine data at 22% N1 as well as 63% N1. The $d_m <$
532 10nm mode was not as prominent in the V2527-A5 engine exhaust at any thrust,
533 although some evidence was observed for it (e.g. number distribution at 40% N1 in
534 Figure 5b). Our data do not allow us to identify whether these small particles were
535 non-volatile or represent an imperfect performance of the CS and TD.

536
537 There is some evidence for an increase in SMPS-calculated volume at larger
538 particle sizes in Figure 5a, at both 40% and 60% N1. If these large particles
539 indicated the presence of a large aerosol mode which varied independently from
540 the primary mode (e.g. if they were emitted by some other process than the engine
541 itself), they would introduce a EI_m -dependent bias in the ratio of SMPS-based EI_m
542 to other instruments, which was not observed (Section 4.4.2).

543
544 Since the CFM56-2C1-with-JP-8 data were strongly influenced by a nucleation
545 mode, and were therefore not well described by the GMD and GSD of the data,
546 these measurements have been omitted from all subsequent PSD analysis in this
547 manuscript. Bimodal fits to the data were not possible as the nucleation mode was
548 not captured by our size distributions. However, the nvPM mass measurements
549 are much less sensitive to these small particles (Hinds, 1999) and have therefore
550 been retained. PSDs from all instruments, test points, and fuels from both the
551 CFM56-2C1 and V2527-A5 engines are included in the [Data Availability section](#).

Deleted: supplement

553 4.2.3 Particle size statistics; GMD and GSD

554 Figure 6 summarizes the PSDs measured by three instruments in terms of their
555 GMD and GSD. The data sets labelled SMPS and TD-SMPS were both obtained from
556 NASA's SMPS, which was manually switched to a bypass line and the TD at each
557 test point. The data set labelled CS-SMPS was obtained with NRC's SMPS.

558 Total PM is represented by the data sets labelled DMS500 and SMPS. However, the
559 two are not directly comparable because the DMS500 measurements were
560 obtained after an additional dilution by a factor of 4 in the NARS and the DMS500
561 was not operated behind a volatile particle remover (CS or TD). Moreover, the
562 inversion of DMS500 data requires more assumptions about the particle size
563 distribution than the analogous SMPS calculation. Either volatiles or this inversion
564 procedure may have caused the 10% larger GSDs observed for the DMS500 for
565 some data (some measurements with GMDs over 35 nm) relative to the SMPS.
566 Since volatiles would affect both GMD and GSD, but we primarily observed
567 discrepancies in the DMS500 GSD, we suggest that the inversion was the major
568 source of bias in these data.

569
570 nvPM is represented by the open circles and filled squares in Figure 6. These two
571 data sets show a different relationship (slope) between GMD and GSD, reflecting
572 systematic differences in the corresponding PSDs. Relative to the mean of the two
573 instruments, the NRC GMDs were higher (Figure 7a) while the NRC GSDs were
574 higher at $GSD < 1.75$ but lower at $GSD > 1.75$ (Figure 7b). Inspection of the
575 corresponding PSDs showed that the NASA and NRC instruments agreed at higher
576 d_m but that NRC number concentrations were higher at smaller d_m . This trend
577 suggests that a bias in the penetration functions applied to each instrument
578 (Figure 4, Table 2) led to the discrepancy in GMD and GSD. Such a bias would affect
579 the nvPM concentration estimated from these PSDs (Figure 8b) and will be
580 discussed further below.

581 In spite of these trends in GMD and GSD, the PSD measurements agreed to within
582 20% (Figure 7a) for nvPM GMDs and within 5% for nvPM GSDs (Figure 7b).
583 Furthermore, these measurements are consistent with previous measurements by

584 Lobo et al. (2015c), as illustrated by the line in Figure 6, which reproduces the
585 polynomial best-fit line reported by those authors.

586 *4.3 Consistency between number-based emission indices of nvPM and*
587 *vPM*

588 Figure 7c compares the measured vPM and nvPM EI_{num} with the mean nvPM EI_{num}
589 (i.e., mean of the NRC CS-SMPS, NASA TD-SMPS, and NARS APC. The grey shading
590 shows that all instruments agreed to within a factor of 2. The APC and DMS500
591 nvPM EI_{num} were both typically higher than the two similar SMPSs. Substantial
592 variability between the two SMPSs was also observed.

593
594 In Figure 7c, the penetration-corrected APC EI_{num} are approximately 50% larger
595 than the SMPS EI_{num} under all conditions. Our measured PSDs rule out the
596 possibility that 50% of particles were not seen by the SMPS. Therefore, we
597 attribute the difference between APC and SMPS results to uncertainties in the APC
598 or SMPS penetration correction functions (Figure 4), i.e., we hypothesize that this
599 difference would not have been observed had the instruments all sampled from
600 the same plenum from comparable sampling lines.

601 We also attribute the larger nvPM EI_{num} measured by the DMS500 to the same
602 cause; to which a similar penetration function as the APC applies (Section 3.4.2).
603 We note that the DMS500 measured total PN, not nvPN, so is expected to report
604 higher number concentrations when volatile particles are present.

605 *4.4 Consistency between mass-based emission indices*

606 *4.4.1 EI_m measurements by real-time sampling instruments*

607 Figure 8a presents scatterplots of the real-time EI_m measurements acquired during
608 this study for all fuels and both engine types. In Figure 8a, the individual EI_m are
609 plotted against the geometric mean of the instruments shown in the caption: three
610 LII 300 instruments, two CAPS instruments, one PAX and one MSS+. The geometric
611 mean was chosen over the more-common arithmetic mean because the data are
612 not normally distributed; the arithmetic mean would therefore have over-

613 emphasized outliers.

614 Figure 9a presents the same data as Figure 8a except that the ordinate data have
615 been normalized to the geometric-mean El_m from Figure 8a. Most data fall within
616 30 % of the mean (inner dashed lines) above 100 mg / kg_{fuel}. We note that exhaust
617 samples were diluted with background air by a factor of 40 or more before
618 reaching the inlet probe, so at this lower limit, the actual concentration observed
619 by the instruments was approximately 10 $\mu\text{g m}^{-3}$ (the exact conversion factor
620 varies with CO₂ concentration and fuel properties), which is close to their
621 detection limits, as expected. This lower limit may have been influenced by the
622 ambient measurement conditions, where background nvPM concentrations were
623 non-negligible.

624 The agreement of the real-time measurements to within 30 % is larger than the
625 calibration uncertainties of the individual instruments, and suggests an influence
626 of systematic biases (e.g. in instrument calibration or penetration corrections).
627 There is no evidence of systematic differences between absorption and LII
628 measurements, which might have been hypothesized if coatings of volatile PM on
629 the light-absorbing nvPM had enhanced absorption. The larger scatter at lower
630 El_m values reflects the noise levels of the instruments. Both of these observations
631 are consistent with data reported previously for different engine types by Lobo et
632 al. (2016, 2020). The LII 300 and MSS+ from the North American Reference System
633 (NARS) have been widely used to characterize aircraft engine nvPM emissions. The
634 two CAPS instruments were independently calibrated and operated. The MSS+ and
635 PAX represent two photoacoustic spectrometers from different manufacturers,
636 operated by different teams, with different principles of calibration. The PAX was
637 also operated with a damaged capacitor on its printed circuit board. As noted in
638 Methods, these instruments operate on a variety of physical principles, including
639 photoacoustic spectroscopy (with two different designs), extinction-minus-
640 scattering, and laser-induced incandescence (cf. Section 3.3.3). Agreement
641 between these various principles also suggests that factors such as volatile
642 coatings on nvPM did not influence the instrument responses.

643 4.4.2 SMPS-based El_m

644 Figure 8b and Figure 9b are analogous to Figure 8a and Figure 9a, but for the
645 integrative nvPM measurements that do not fall into the real-time sampling
646 category. These data are plotted against the same geometric mean from Figure 8a.
647 The dashed lines in Figure 9b represent the same ratios as in Figure 9a.
648 Considering that the real-time instruments in Figure 8a were either calibrated to
649 aerosol absorption or to aviation nvPM, we consider their accuracy as greater than
650 the instruments in Figure 8b and consider departures from the 1:1 line as due to
651 inaccuracy.

652 Most of the instruments in Figure 8b were accurate to within 30% of the reference,
653 similar to Figure 8a, with the exception of the CS-SMPS and PSAP. This is
654 summarized in Table 3, which shows the mean ratios of all data except engine idle
655 (23% N1) with the geometric mean. Table 3 also includes the results of a linear
656 regression against the geometric mean to facilitate comparison of our
657 measurements with Kinsey et al. (2021), who performed linear regressions against
658 simultaneous elemental carbon (EC) measurements (in our study, mass
659 concentrations were too low to obtain EC measurements). The PSAP data are
660 discussed in the next section. The CS-SMPS data were systematically higher than
661 the geometric mean, potentially due to an overcorrection of the penetration of
662 large particles to the SMPS or due to uncertainty in the effective density that must
663 be assumed when converting SMPS data to El_m . As noted in Section 3.3.3, we
664 assumed an effective density of 1000 kg m^{-3} based on the work of Durdina et al.
665 (2014). Considerable uncertainty could be introduced due to this assumption, as
666 the effective density of the nvPM particles (Momenimovahed and Olfert, 2015)
667 may vary with the monomer diameter (Abegglen et al., 2014; Durdina et al., 2014)
668 and/or shape of soot aggregates. With respect to the real-time measurements, the
669 TD-SMPS data are also consistent with previous measurements of aviation engine
670 PSDs, which, however, were not corrected for diffusional particle loss (Lobo et al.,
671 2015b, 2020).

Formatted: Subscript

Deleted: ¶

Since the spread of nvPM El_m reported by the two SMPS systems was smaller than the bias, their difference relative to the reference El_m cannot be attributed to measurement biases (such as the limited size range detected by the instruments). Since the two SMPS systems showed different accuracies, their differences cannot be ascribed to a lack of constraints on the effective density of the nvPM particles (Momenimovahed and Olfert, 2015), which may vary with the monomer diameter (Abegglen et al., 2014; Durdina et al., 2014) and/or shape of soot aggregates. (We reiterate that our assumption of constant effective density is expected to introduce negligible uncertainty for the small soot particles emitted by aircraft turbine engines; Durdina et al., 2014).

Deleted: Careful measurement of the penetration functions used in these calculations would be required to confirm our interpretation.

690 4.4.3 *Filter photometer-based El_m from TAP and PSAP*

691 Figure 8b and Figure 9b show that the TAP measurements were within the 30 %
692 range observed for the real-time instruments, with a relative standard deviation
693 (RSD) of 14 % (Table 3) for all data excluding the engine idle condition (23% N1).
694 This provides high confidence for the use of the TAP for in-flight or field
695 measurements of aircraft-engine nvPM mass emissions, when filter-loading
696 corrections (Section 3.3.3) are correctly applied.

697 The PSAP, on the other hand, showed much greater variability, with an RSD of 36%
698 (Table 3). This is substantially higher than the variability reported by a laboratory
699 intercomparison of PSAP and CAPS PM₅₅ (Perim De Faria et al., 2021) (that study
700 did not report a statistic comparable to RSD). Although the PSAP has been
701 observed to deviate up to a factor of two higher in cases of high organic aerosol
702 loading or reduced filter transmission (Lack et al., 2013), our data are restricted to
703 transmissions above 0.8. The fact that the PSAP shows great variability rather than
704 a fixed offset indicates that the issue is not due to a systematic error such as an
705 inaccurate MAC or flow rate calibration. We note that the TAP and PSAP were
706 operated with reduced sample flow rates of 0.05 L min⁻¹ and 0.1 L min⁻¹,
707 respectively, (5 to 10% of nominal settings) to extend the life of their filter media
708 while sampling the high soot concentrations in the aircraft exhaust. Under these
709 conditions, detector noise and small fluctuations in sample flow have a magnified
710 effect on resulting derived absorption coefficients. We suspect that the
711 measurements would have been significantly more precise if the instruments had
712 been operated at nominal flows, although this would have required changing
713 filters after each test point. Consistent with our hypothesis, we note that
714 Nakayama et al. (2010) observed substantially larger variability in PSAP
715 measurements at 0.3 than at 0.7 standard litres per minute. We also note that Bond
716 et al. (1999) did not observe an impact of flow rate when changing from 1 to 2
717 litres per minute.

718 Figure 10 plots as a function of particle GMD the same relative TAP and PSAP El_m
719 data shown in Figure 9b. No clear trend of this ratio with size is evident, although
720 the measurements become somewhat more scattered at smaller sizes for the SAF1

721 data set, where signal to noise is lower (GMD and EI_m were correlated, see the
722 below discussion of Figure 12). Figure 10b includes the size-dependent PSAP
723 correction function reported by Nakayama et al. (2010) (their Equation 8), with
724 shading representing a 1σ uncertainty. Those authors predicted the true
725 absorption values using Mie theory for nigrosin particles of diameter 100 to
726 600 nm and refractive index 1.685–0.285*i*. Thus, their correction factor is
727 conceptually equivalent to our EI_m /mean- EI_m . Extrapolating their correction
728 function down from 100 nm to 15 nm gives values ranging from 4 to 8, whereas
729 our measurements are close to 1.0. This discrepancy may be attributed primarily
730 to the extrapolation, and possibly also to the fact that we have measured solid
731 nvPM particles rather than liquid nigrosin. Overall, it is clear that the variability in
732 our PSAP data is not sufficiently predicted by the GMD.

733 Overall, our data show that any possible size dependency in the TAP and PSAP
734 response is smaller than the observed variability between samples. The TAP and
735 PSAP data exhibit relative standard deviations (RSD) of 19% and 16%,
736 respectively, for samples with GMD > 25 nm. Future studies may consider
737 correcting PSAP and TAP measurements by the ratios shown in Table 3, if they are
738 operated at similarly modified flow rates. The ratios in Table 3, represent the ratio
739 between the calibrated aerosol-phase nvPM mass measurements and the
740 previously uncalibrated PSAP and TAP measurements, for data above 25 mg kg_{fuel}⁻¹
741 and N1 > 40% and for respective flow rates at 5% and 10% of the nominal values.

Deleted: which

742 4.5 Instrument performance for fuels with different composition

743 Figure 11 shows a category plot of the ratio EI_m /mean- EI_m (that is, the ordinate of
744 Figure 9) for the different instruments. Data below 100 mg / kg_{fuel} have been
745 excluded as this ratio reflects only noise in that region (Figure 9). The symbols
746 have been sized by mean N1. The data have been coded by symbol and colour to
747 reflect the 6 fuels used in this study, although JP-8 measurements are few in
748 number due to the EI_m of the data set (CFM56-2C1 with JP-8) being typically below
749 25 mg / kg_{fuel}.

750 Figure 11 shows that no substantial difference can be seen for these instruments

752 for the nvPM E_{lm} for fuels with different composition; the spread in the data for a
753 given fuel is larger than the difference between fuels. Outliers tend to be associated
754 with low N₁ (small symbols). Because low N₁ corresponds to both lower
755 concentrations (lower signal-to-noise) and lower exhaust velocities relative to
756 ambient wind speeds, these outliers are not surprising.

757 The instruments in Figure 11 show a linear response to nvPM mass and operate on
758 a range of physical principles. This observation indicates that no instrument was
759 uniquely sensitive to changes in particle size over the observed range, since E_{lm}
760 was correlated with GMD (Figure 12), as is typical of aviation engines (Saffaripour
761 et al., 2020). We note that the response of all of these instruments is proportional
762 to the MAC of the sample, so that it remains possible that the sample MAC changed
763 with GMD or E_{lm}.

764 4.6 *Influence of LII laser fluence*

765 An additional experiment was performed to test the hypothesis that the laser
766 fluence of the LII 300 may not be sufficiently high to heat nvPM to incandescence
767 in aircraft-engine PM emissions from SAFs at different engine thrusts. The
768 experimental design was similar to that of Yuan et al. (2022). This hypothesis is
769 related to electron microscopy evidence (Vander Wal et al., 2014) showing that the
770 degree of graphitization of aircraft-engine soot may be substantially lowered at
771 low thrusts. A lower degree of graphitization may result in a lower LII signal if the
772 1064 nm MAC is lower (resulting in a lower maximum temperature being reached)
773 or if part of the laser energy leads to carbon annealing rather than thermal
774 excitation (Botero et al., 2021; Ugarte, 1992; Vander Wal and Choi, 1999). If
775 correct, this hypothesis would mean that the nvPM concentrations reported by an
776 LII 300 operated at reduced fluence would be lower than those of a reference LII
777 300. Higher fluences are also required for nvPM internally mixed with volatile PM,
778 as some laser energy may be lost to volatile evaporation (Michelsen et al., 2015).

779 Figure 13a illustrates the experiment we performed to test this hypothesis. The
780 figure presents data for SAF1 only; results for other fuels were similar. One
781 “reduced-fluence” LII 300 was programmed to change its Q-switch delay from

782 140 μ s to 240 μ s, with a randomized order. In this experiment, lower Q-switch
783 delays corresponded to higher laser fluence; the lowest Q-switch delay was the
784 optimal one for this system. Another “reference” LII 300 operated with no change
785 to its Q-switch delay. Figure 13a shows that the reduced-fluence LII reported lower
786 mass concentrations when its Q-switch delay was increased, but returned to the
787 expected values when its Q-switch delay was reduced.

788 We defined R_{LII} as the ratio of nvPM mass concentrations reported by the reduced-
789 fluence and reference LII 300 instruments. Figure 13b shows that R_{LII} was a
790 function of Q-switch delay, and therefore laser fluence, for all engine thrust
791 conditions. This observation is expected, since LII signals are lower at lower
792 fluence (Michelsen et al., 2015) and since we calculated R_{LII} without taking this
793 effect into account. We have verified in our laboratory that Q-switch delay is
794 inversely proportional to laser fluence for this system and that saturation effects
795 are negligible.

796 A trend of decreasing R_{LII} with decreasing N1 is evident at moderate and low Q-
797 switch delays, which can be interpreted as indicating that the nvPM was more
798 graphitic at higher N1 conditions ([Vander Wal et al., 2014](#); [Liati et al., 2014](#)).

799 However, R_{LII} reached a plateau at high fluence (smaller Q-switch delay), which is
800 the region where the LII 300 normally operates. This plateau was reached at all
801 engine thrusts, with a broader range for the plateau at higher thrusts and a
802 decreasing range as the thrust was lowered. Therefore, the LII 300 has sufficient
803 fluence and can be expected to perform well for SAF blends at all engine thrust
804 conditions.

805 5 Conclusions

806 For multiple instruments measuring nvPM number, size, and mass, we observed
807 no evidence of anomalous instrument responses to the exhaust emissions
808 produced by SAF blends relative to petroleum jet fuel (REFs) combustion in an IAE
809 V2527-A5 engine. The GMD, GSD, and EI_{num} data for all fuels fell within 20%, 5%,
810 and a factor of 2 of their mean, respectively. Anomalous instrumental responses
811 would have resulted in two groups of data for these parameters, which was not
812 observed. However, a difference between EI_{num} for instruments located on

813 different-length sampling lines was noted and attributed to a greater sensitivity of
814 EI_{num} than EI_m to the penetration function.

815
816 The majority of nvPM mass measurements by the real-time instruments (CAPS
817 PMSSA, LII 300, MSS+, PAX) agreed to within 30% of their geometric mean
818 (reference mean), for EI_m above 100 mg/ kg_{fuel}. This lower limit corresponded to a
819 mass concentration of approximately 10 $\mu\text{g m}^{-3}$ (the conversion of EI_m to mass
820 varies because the emitted [CO₂] varies), which was the noise level of these
821 instruments in our sampling setup. The ratio of each real-time measurement with
822 the reference mean was close to unity (maximally 1.24, minimally 0.78) and
823 indicated good precision (all RSDs \leq 17%).

824
825 Integrative nvPM EI_m , calculated from PSD measurements or filter attenuation
826 (TAP and PSAP), fell within a factor of two of the reference mean. The ratio of each
827 integrative measurement with the reference mean was further from unity
828 (maximally 1.50, minimally 0.88) and variability was higher precision (all RSDs
829 \leq 36%). The variability in TAP data was notably low at 14%, and the variability in
830 PSAP data was notably high at 36%, likely due to its operation at a reduced flow
831 rate (as noted, the TAP and PSAP were operated at 5% and 10% of their nominal
832 flow rates, respectively).

833
834 Two other instrument- and fuel composition-specific observations were made. A
835 dedicated experiment showed that changing the laser fluence of an LII 300 could
836 influence its reported nvPM mass concentrations at low to moderate fluences. By
837 maintaining sufficiently high fluence a plateau region was established, irrespective
838 of thrust or fuel, where reported nvPM mass concentrations were stable and not
839 influenced by experimental conditions. Second, additional measurements of
840 emissions from JP-8 fuel combusted in a CFM56-2C1 engine indicated the presence
841 of very high concentrations of volatile nucleation-mode particles with
842 diameter < 20 nm. These measurements reflect a different engine, as well as a fuel
843 with a factor 20 higher sulfur content, and the increased total PM number
844 concentration is most likely attributable to the sulfur.

845

846 Overall, this study found that real-time instruments for the measurement of nvPM
847 emissions in aviation turbine engines are comparable whether conventional fuels
848 or SAFs are used. Since all real-time measurements were influenced by the MAC
849 and no independent measurement of nvPM mass was made, no conclusions about
850 the variability thereof can be made from this study.

851 5.1 *Author contributions*

852 BEA, PLC, TS, PL, GJS, PDW, and RML designed the study. JCC, TS, PLC, GJS, ECC, SA,
853 PDW, RML, ZY, AF, MT, DS, WL, CR, PO, MS, and PL took the measurements. JCC, TS,
854 BEA, RHM, MAS, ECC, SA, ZY analyzed the data with input from GJS, PL, RML, and
855 AF. JCC prepared the figures. JCC and PL drafted the manuscript. All authors
856 discussed the data interpretation and presentation.

857 5.2 *Competing interests*

858 RML and AF are employed by [Aerodyne Research Inc.](#), which produces the CAPS
859 PMSSA commercially. ZY was employed by [Aerodyne Research Inc.](#) at the time of the
860 study.

Deleted: ARI

Deleted: ARI

861 5.3 *Acknowledgements*

862 We acknowledge the efforts of the flight and ground crews of the DLR ATRA, the
863 NASA DC8, and the U.S. Air Force 86th Air Wing. We thank the ground staff of
864 Ramstein Air Base for their operational support during this experiment.

865 5.4 *Financial support*

866 This research received funding from the Transport Canada project "TC Aviation —
867 nvPM from renewable and conventional fuels". The campaign was funded by the
868 DLR aeronautics program in the framework of the project "Emission and Climate
869 Impact of Alternative Fuels (ECLIF)". MS&T and ARI received support from the U.S.
870 Federal Aviation Administration (FAA) through the Aviation Sustainability Center
871 (ASCENT) – a U.S. FAA-NASA- U.S. DoD-Transport Canada- U.S. EPA sponsored
872 Center of Excellence for Alternative Jet Fuels and Environment under Grant No. 13-
873 C-AJFE-MST, Amendment 010. A.F. was supported by funds from ARI. ATRA
874 operational and fuel costs along with DLR scientists' participation was funded by
875 the DLR aeronautics program in the framework of the project "Emission and
876 Climate Impact of Alternative Fuels (ECLIF)". The U.S. FAA Office of Environment
877 and Energy and the National Aeronautics and Space Administration Aeronautics
878 Research Mission Directorate supported field and DC-8 operations, and

881 participation of the U.S. researchers in the project.

882 **5.5 Data availability**

883 The data presented in Figures 4 to 10 are available in the Zenodo repository at
884 <https://doi.org/10.5281/zenodo.5504098>, as a spreadsheet file. Other data are
885 available from the authors upon request.

Deleted: <https://sandbox.zenodo.org/record/950512>

886 **6 References**

887 [Durdina, L., Brem, B. T., Elser, M., Schönenberger, D., Siegerist, F., & Anet, J. G. \(2021\). Reduction of Nonvolatile Particulate Matter Emissions of a Commercial](https://doi.org/10.1021/acs.est.1c04744)
888 [Turbofan Engine at the Ground Level from the Use of a Sustainable Aviation Fuel Blend. Environmental Science & Technology, 55\(21\), 14576–14585.](https://doi.org/10.1021/acs.est.1c04744)
889 <https://doi.org/10.1021/acs.est.1c04744>

Formatted: Line spacing: single

890 [vander Wal, R. L., Bryg, V. M., & Huang, C. H. \(2014\). Aircraft engine particulate matter: Macro- micro- and nanostructure by HRTEM and chemistry by XPS. Combustion and Flame, 161\(2\), 602–611.](https://doi.org/10.1016/j.combustflame.2013.09.003)
891 <https://doi.org/10.1016/j.combustflame.2013.09.003>

892 [Lati, A., Brem, B. T., Durdina, L., Vögeli, M., Dasilva, Y. A. R., Eggenschwiler, P. D., & Wang, J. \(2014\). Electron Microscopic Study of Soot Particulate Matter Emissions from Aircraft Turbine Engines. Environmental Science & Technology, 48\(18\), 10975–10983. https://doi.org/10.1021/es501809b](https://doi.org/10.1021/10501809b)

Formatted: Paragraph

900
901 ASTM D4054: Practice for Evaluation of New Aviation Turbine Fuels and Fuel Additives. Conshohocken, PA: ASTM International; 2019. doi: 10.1520/D4054-19.

902
903 ASTM D7566: Specification for Aviation Turbine Fuel Containing Synthesized Hydrocarbons. Conshohocken, PA: ASTM International; 2020. doi: 10.1520/D7566-20

904
905 International Civil Aviation Organization (2017). International Standards and Recommended Practices – Annex 16 to the Convention on International Civil Aviation: Environmental Protection, Volume II - Aircraft Engine Emissions, 4th ed., Montreal, QC, Canada.

906
907 Abegglen, M., Durdina, L., Mensah, A., Brem, B., Corbin, J., Wang, J., Lohmann, U. and Sierau, B.: Effective density measurements of fresh particulate matter emitted by an aircraft engine, in EGU General Assembly Conference Abstracts, vol. 16, p. 14367., 2014.

908
909 ASTM D4054: Practice for Evaluation of New Aviation Turbine Fuels and Fuel Additives. Conshohocken, PA: ASTM International; 2019. doi: 10.1520/D4054-19.

910
911 ASTM D7566: Specification for Aviation Turbine Fuel Containing Synthesized Hydrocarbons. Conshohocken, PA: ASTM International; 2020. doi: 10.1520/D7566-20

912
913 Beyersdorf, A. J., Timko, M. T., Ziembka, L. D., Bulzan, D., Corporan, E., Herndon, S. C., Howard, R., Miake-Lye, R., Thornhill, K. L., Winstead, E., Wey, C., Yu, Z. and Anderson, B. E.: Reductions in aircraft particulate emissions due to the use of Fischer-Tropsch fuels,

920 Atmos. Chem. Phys., 14(1), 11–23, doi:10.5194/acp-14-11-2014.

921 Bond, T. C. and Bergstrom, R. W.: Light absorption by carbonaceous particles: An
922 investigative review, *Aerosol Sci. Technol.*, 40(1), 27–67,
923 doi:10.1080/02786820500421521, 2006.

924 Bond, T. C., Anderson, T. L. and Campbell, D.: Calibration and Intercomparison of Filter-
925 Based Measurements of Visible Light Absorption by Aerosols, *Aerosol Sci. Technol.*, 30(6),
926 582–600, doi:10.1080/027868299304435, 1999.

927 Botero, M. L., Akroyd, J., Chen, D., Kraft, M. and Agudelo, J. R.: On the thermophoretic
928 sampling and TEM-based characterisation of soot particles in flames, *Carbon N. Y.*, 171,
929 711–722, doi:10.1016/j.carbon.2020.09.074, 2021.

930 Brem, B. T., Durdina, L., Siegerist, F., Beyerle, P., Bruderer, K., Rindlisbacher, T., Rocci-
931 Denis, S., Andac, M. G., Zelina, J., Penanhoat, O. and Wang, J.: Effects of Fuel Aromatic
932 Content on Nonvolatile Particulate Emissions of an In-Production Aircraft Gas Turbine,
933 *Environ. Sci. Technol.*, 49(22), 13149–13157, doi:10.1021/acs.est.5b04167, 2015.

934 Cain, J., Dewitt, M. J., Blunck, D., Corporan, E., Striebich, R., Anneken, D., Klingshirn, C.,
935 Roquemore, W. M. and Vander Wal, R.: Characterization of gaseous and particulate
936 emissions from a turboshaft engine burning conventional, alternative, and surrogate fuels,
937 *Energy Fuels*, 27(4), 2290–2302, doi:10.1021/ef400009c, 2013.

938 Catalytic Stripper CS015 Instrument Manual, Catalytic Instruments GmbH, 2014.

939 Clarke, A. D.: A thermo-optic technique for in situ analysis of size-resolved aerosol
940 physicochemistry, *Atmos. Environ. Part A, Gen. Top.*, 25(3–4), 635–644,
941 doi:10.1016/0960-1686(91)90061-B, 1991.

942 Corporan, E., Edwards, T., Shafer, L., Dewitt, M. J., Klingshirn, C., Zabarnick, S., West, Z.,
943 Striebich, R., Graham, J. and Klein, J.: Chemical, thermal stability, seal swell, and emissions
944 studies of alternative jet fuels, *Energy Fuels*, 25(3), 955–966, doi:10.1021/ef101520v,
945 2011.

946 Durand, E., Lobo, P., Crayford, A., Sevcenco, Y. and Christie, S.: Impact of fuel hydrogen
947 content on non-volatile particulate matter emitted from an aircraft auxiliary power unit
948 measured with standardised reference systems, *Fuel*, 287, 119637,
949 doi:10.1016/j.fuel.2020.119637, 2021.

950 Durdina, L., Brem, B. T., Abegglen, M., Lobo, P., Rindlisbacher, T., Thomson, K. A.,
951 Smallwood, G. J., Hagen, D. E., Sierau, B. and Wang, J.: Determination of PM mass emissions
952 from an aircraft turbine engine using particle effective density, *Atmos. Environ.*, 99, 500–
953 507, doi:10.1016/j.atmosenv.2014.10.018, 2014.

954 Elser, M., Brem, B. T., Durdina, L., Schönenberger, D., Siegerist, F., Fischer, A. and Wang, J.:
955 Chemical composition and radiative properties of nascent particulate matter emitted by
956 an aircraft turbofan burning conventional and alternative fuels, *Atmos. Chem. Phys.*,
957 19(10), 6809–6820, doi:10.5194/acp-19-6809-2019, 2019.

958 Gagné, S., Couillard, M., Gajdosechova, Z., Momenimovahed, A., Smallwood, G., Mester, Z.,
959 Thomson, K., Lobo, P. and Corbin, J. C.: Ash-Decorated and Ash-Painted Soot from Residual
960 and Distillate-Fuel Combustion in Four Marine Engines and One Aviation Engine, *Environ.*
961 *Sci. Technol.*, 55, 6584–6593, doi:10.1021/acs.est.0c07130, 2021.

962 Hileman, J. I. and Stratton, R. W.: Alternative jet fuel feasibility, *Transp. Policy*, 34, 52–62,
963 doi:10.1016/j.tranpol.2014.02.018, 2014.

964 Hinds, W. C.: *Aerosol technology: properties, behavior, and measurement of airborne
965 particles*, John Wiley & Sons., 1999.

966 Huang, C. H. and Vander Wal, R. L.: Effect of soot structure evolution from commercial jet
967 engine burning petroleum based JP-8 and synthetic HRJ and FT fuels, *Energy Fuels*, 27(8),
968 4946–4958, doi:10.1021/ef400576c, 2013.

969 ICAO: International Standards and Recommended Practices – Annex 16 to the Convention
970 on International Civil Aviation: Environmental Protection, Volume II - Aircraft Engine
971 Emissions, Montreal, QC, 2017.

972 International Civil Aviation Organization (2017). International Standards and
973 Recommended Practices – Annex 16 to the Convention on International Civil Aviation:
974 Environmental Protection, Volume II - Aircraft Engine Emissions, 4th ed., Montreal, QC,
975 Canada.

976 Kiliç, D., El Haddad, I., Brem, B. T., Bruns, E., Bozetti, C., Corbin, J., Durdina, L., Huang, R. J.,
977 Jiang, J., Klein, F., Lavi, A., Pieber, S. M., Rindlisbacher, T., Rudich, Y., Slowik, J. G., Wang, J.,
978 Baltensperger, U. and Prévôt, A. S. H.: Identification of secondary aerosol precursors
979 emitted by an aircraft turbofan, *Atmos. Chem. Phys.*, 18(10), 7379–7391, doi:10.5194/acp-
980 18-7379-2018, 2018.

981 Kinsey, J. S., Timko, M. T., Herndon, S. C., Wood, E. C., Yu, Z., Miake-Lye, R. C., Lobo, P.,
982 Whitefield, P., Hagen, D., Wey, C., Anderson, B. E., Beyersdorf, A. J., Hudgins, C. H., Thornhill,
983 K. L., Edward, W., Howard, R., Bulzan, D. I., Tacina, K. B. and Knighton, W. B.: Determination
984 of the emissions from an aircraft auxiliary power unit (APU) during the alternative
985 aviation fuel experiment (AAFEX), *J. Air Waste Manag. Assoc.*, 62(4), 420–430,
986 doi:10.1080/10473289.2012.655884, 2012.

987 Kinsey, J. S., Giannelli, R., Howard, R., Hoffman, B., Frazee, R., Aldridge, M., Leggett, C.,
988 Stevens, K., Kittelson, D., Silvis, W., Stevens, J., Lobo, P., Achterberg, S., Swanson, J.,
989 Thomson, K., McArthur, T., Hagen, D., Trueblood, M., Wolff, L., Liscinsky, D., Arey, R.,
990 Cerully, K., Miake-Lye, R., Onasch, T., Freedman, A., Bachalo, W., Payne, G. and Durlicki, M.:
991 Assessment of a regulatory measurement system for the determination of the non-volatile
992 particulate matter emissions from commercial aircraft engines, *J. Aerosol Sci.*, 154,
993 105734, doi:10.1016/j.jaerosci.2020.105734, 2021.

994 Kumal, R. R., Liu, J., Gharpure, A., Vander Wal, R. L., Kinsey, J. S., Giannelli, B., Stevens, J.,
995 Leggett, C., Howard, R., Forde, M., Zelenyuk, A., Suski, K., Payne, G., Manin, J., Bachalo, W.,
996 Frazee, R., Onasch, T. B., Freedman, A., Kittelson, D. B. and Swanson, J. J.: Impact of Biofuel
997 Blends on Black Carbon Emissions from a Gas Turbine Engine, *Energy Fuels*, 34(4), 4958–
998 4966, doi:10.1021/acs.energyfuels.0c00094, 2020.

999 Lack, D. A., Moosmüller, H., McMeeking, G. R., Chakrabarty, R. K. and Baumgardner, D.:
1000 Characterizing elemental, equivalent black, and refractory black carbon aerosol particles:
1001 a review of techniques, their limitations and uncertainties, *Anal. Bioanal. Chem.*, 406(1),
1002 99–122, doi:10.1007/s00216-013-7402-3, 2014.

1003 Liati, A., Schreiber, D., Alpert, P. A., Liao, Y., Brem, B. T., Corral Arroyo, P., Hu, J., Jonsdottir,
1004 H. R., Ammann, M. and Dimopoulos Eggenschwiler, P.: Aircraft soot from conventional
1005 fuels and biofuels during ground idle and climb-out conditions: Electron microscopy and
1006 X-ray micro-spectroscopy, *Environ. Pollut.*, 247, 658–667,
1007 doi:10.1016/j.envpol.2019.01.078, 2019.

1008 Liu, F., Yon, J., Fuentes, A., Lobo, P., Smallwood, G. J. and Corbin, J. C.: Review of recent
1009 literature on the light absorption properties of black carbon: Refractive index, mass
1010 absorption cross section, and absorption function, *Aerosol Sci. Technol.*, 54(1), 33–51,
1011 doi:10.1080/02786826.2019.1676878, 2020.

1012 Lobo, P., Hagen, D. E. and Whitefield, P. D.: Comparison of PM emissions from a commercial
1013 jet engine burning conventional, biomass, and fischer-tropsch fuels, *Environ. Sci. Technol.*,
1014 45(24), doi:10.1021/es201902e, 2011.

1015 Lobo, P., Christie, S., Khandelwal, B., Blakey, S. G. and Raper, D. W.: Evaluation of Non-
1016 volatile Particulate Matter Emission Characteristics of an Aircraft Auxiliary Power Unit
1017 with Varying Alternative Jet Fuel Blend Ratios, *Energy Fuels*, 29(11), 7705–7711,
1018 doi:10.1021/acs.energyfuels.5b01758, 2015a.

1019 Lobo, P., Durdina, L., Smallwood, G. J., Rindlisbacher, T., Siegerist, F., Black, E. A., Yu, Z.,
1020 Mensah, A. A., Hagen, D. E., Miake-Lye, R. C., Thomson, K. A., Brem, B. T., Corbin, J. C.,
1021 Abegglen, M., Sierau, B., Whitefield, P. D. and Wang, J.: Measurement of aircraft engine non-
1022 volatile PM emissions: Results of the Aviation-Particle Regulatory Instrumentation
1023 Demonstration Experiment (A-PRIDE) 4 campaign, *Aerosol Sci. Technol.*, 49(7), 472–484,
1024 doi:10.1080/02786826.2015.1047012, 2015b.

1025 Lobo, P., Hagen, D. E., Whitefield, P. D. and Raper, D.: PM emissions measurements of in-
1026 service commercial aircraft engines during the Delta-Atlanta Hartsfield Study, *Atmos.*
1027 *Environ.*, 104, 237–245, doi:10.1016/j.atmosenv.2015.01.020, 2015c.

1028 Lobo, P., Condevaux, J., Yu, Z., Kuhlmann, J., Hagen, D. E., Miake-Lye, R. C., Whitefield, P. D.
1029 and Raper, D. W.: Demonstration of a Regulatory Method for Aircraft Engine Nonvolatile
1030 PM Emissions Measurements with Conventional and Isoparaffinic Kerosene fuels, *Energy*
1031 *Fuels*, 30(9), 7770–7777, doi:10.1021/acs.energyfuels.6b01581, 2016.

1032 Lobo, P., Durdina, L., Brem, B. T., Crayford, A. P., Johnson, M. P., Smallwood, G. J., Siegerist,
1033 F., Williams, P. I., Black, E. A., Llamedo, A., Thomson, K. A., Trueblood, M. B., Yu, Z., Hagen, D.
1034 E., Whitefield, P. D., Miake-Lye, R. C. and Rindlisbacher, T.: Comparison of standardized
1035 sampling and measurement reference systems for aircraft engine non-volatile particulate
1036 matter emissions, *J. Aerosol Sci.*, 145, 105557, doi:10.1016/j.jaerosci.2020.105557, 2020.

1037 Masiol, M. and Harrison, R. M.: Aircraft engine exhaust emissions and other airport-related
1038 contributions to ambient air pollution: A review, *Atmos. Environ.*, 95, 409–455,
1039 doi:10.1016/j.atmosenv.2014.05.070, 2014.

1040 Michelsen, H. A., Schulz, C., Smallwood, G. J. and Will, S.: Laser-induced incandescence:
1041 Particulate diagnostics for combustion, atmospheric, and industrial applications, *Prog.*
1042 *Energy Combust. Sci.*, 51, 2–48, doi:10.1016/j.pecs.2015.07.001, 2015.

1043 Modini, R. L., Corbin, J. C., Brem, B. T., Irwin, M., Bertò, M., Pileci, R. E., Fetfatzis, P.,
1044 Eleftheriadis, K., Henzing, B., Moerman, M. M., Liu, F., Müller, T. and Gysel-Beer, M.:
1045 Detailed characterization of the CAPS single-scattering albedo monitor (CAPS PM_{ssa}) as a
1046 field-deployable instrument for measuring aerosol light absorption with the extinction-
1047 minus-scattering method, *Atmos. Meas. Tech.*, 14(2), doi:10.5194/amt-14-819-2021,
1048 2021.

1049 Momenimovahed, A. and Olfert, J. S.: Effective Density and Volatility of Particles Emitted
1050 from Gasoline Direct Injection Vehicles and Implications for Particle Mass Measurement,
1051 *Aerosol Sci. Technol.*, 49(11), 1051–1062, doi:10.1080/02786826.2015.1094181, 2015.

1052 Moore, R. H., Thornhill, K. L., Weinzierl, B., Sauer, D., D'Ascoli, E., Kim, J., Lichtenstern, M.,
1053 Scheibe, M., Beaton, B., Beyersdorf, A. J., Barrick, J., Bulzan, D., Corr, C. A., Crosbie, E., Jurkat,
1054 T., Martin, R., Riddick, D., Shook, M., Slover, G., Voigt, C., White, R., Winstead, E., Yasky, R.,
1055 Ziomba, L. D., Brown, A., Schlager, H. and Anderson, B. E.: Biofuel blending reduces particle
1056 emissions from aircraft engines at cruise conditions, *Nature*, 543(7645), 411–415,
1057 doi:10.1038/nature21420, 2017.

1058 Nakayama, T., Kondo, Y., Moteki, N., Sahu, L. K., Kinase, T., Kita, K. and Matsumi, Y.: Size-
1059 dependent correction factors for absorption measurements using filter-based
1060 photometers: PSAP and COSMOS, *J. Aerosol Sci.*, 41(4), 333–343,
1061 doi:10.1016/j.jaerosci.2010.01.004, 2010.

1062 Nakayama, T., Suzuki, H., Kagamitani, S., Ikeda, Y., Uchiyama, A. and Matsumi, Y.:

1063 Characterization of a Three Wavelength Photoacoustic Soot Spectrometer ((PASS)-3) and
1064 a Photoacoustic Extinctiometer ((PAX)), J. Meteorol. Soc. Japan. Ser. {II}, 93(2), 285–308,
1065 doi:10.2151/jmsj.2015-016, 2015.

1066 Ogren, J. A., Wendell, J., Andrews, E. and Sheridan, P. J.: Continuous light absorption
1067 photometer for long-Term studies, Atmos. Meas. Tech., 10(12), 4805–4818,
1068 doi:10.5194/amt-10-4805-2017, 2017.

1069 Onasch, T. B., Massoli, P., Kebabian, P. L., Hills, F. B., Bacon, F. W. and Freedman, A.: Single
1070 Scattering Albedo Monitor for Airborne Particulates, Aerosol Sci. Technol., 49(4), 267–279,
1071 doi:10.1080/02786826.2015.1022248, 2015.

1072 Perim De Faria, J., Bundke, U., Freedman, A., Onasch, T. B. and Petzold, A.: Laboratory
1073 validation of a compact single-scattering albedo (SSA) monitor, Atmos. Meas. Tech., 14(2),
1074 1635–1653, doi:10.5194/amt-14-1635-2021, 2021.

1075 Petzold, A., Ogren, J. A., Fiebig, M., Laj, P., Li, S.-M., Baltensperger, U., Holzer-Popp, T., Kinne,
1076 S., Pappalardo, G., Sugimoto, N., Wehrli, C., Wiedensohler, A. and Zhang, X.-Y.:
1077 Recommendations for the interpretation of “black carbon” measurements, Atmos. Chem.
1078 Phys., 13(16), 8365–8379, doi:10.5194/acp-13-8365-2013, 2013.

1079 SAE International. Aerospace Information Report (AIR) 6241 . Procedure for the
1080 Continuous Sampling and Measurement of Non-Volatile Particle Emissions from Aircraft
1081 Turbine Engines. Warrendale, PA, 2013. <https://doi.org/10.4271/AIR6241>

1082 SAE International. Aerospace Recommended Practice (ARP) 6320 - Procedure for the
1083 Continuous Sampling and Measurement of Non-Volatile Particulate Matter Emissions from
1084 Aircraft Turbine Engines, Warrendale, PA, 2018. <https://doi.org/10.4271/ARP6320>.

1085 SAE International. Aerospace Information Report (AIR) 6504 - Procedure for the
1086 Calculation of Sampling System Penetration Functions and System Loss Correction
1087 Factors, Warrendale, PA, 2017. <https://doi.org/10.4271/AIR6504>

1088 SAE International. Aerospace Recommended Practice (ARP) 6481- Procedure for the
1089 Calculation of Sampling Line Penetration Functions and Line Loss Correction Factors,
1090 Warrendale, PA, 2019. <https://doi.org/10.4271/ARP6481>

1091 Saffaripour, M., Thomson, K. A., Smallwood, G. J. and Lobo, P.: A review on the
1092 morphological properties of non-volatile particulate matter emissions from aircraft
1093 turbine engines, J. Aerosol Sci., 139, doi:10.1016/j.jaerosci.2019.105467, 2020.

1094 Schindler, W., Haisch, C., Beck, H. A., Niessner, R., Jacob, E. and Rothe, D.: A photoacoustic
1095 sensor system for time resolved quantification of diesel soot emissions, SAE Technical
1096 Paper 2004-01-0968, SAE International, doi:10.4271/2004-01-0968, 2004.

1097 Schripp, T., Anderson, B. E., Bauder, U., Rauch, B., Corbin, J. C., Smallwood, G. J., Lobo, P.,
1098 Crosbie, E., Shook, M. E., Miake-Lye, R., Yu, Z., Freedman, A., Whitefield, P. D., Robinson, C.
1099 E., Achterberg, S. L., Köhler, M., Oßwald, P., Grein, T., Sauer, D., Voigt, C., Schlager, H.,
1100 LeClercq, P. Aircraft engine particulate matter and gaseous emissions from sustainable
1101 aviation fuels: results from ground-based measurements during the NASA/DLR Campaign
1102 ECLIF2/ND-MAX. Submitted to Fuel. 2022.

1103 Schripp, T., Anderson, B., Crosbie, E. C., Moore, R. H., Herrmann, F., Oßwald, P., Wahl, C.,
1104 Kapernaum, M., Köhler, M., Le Clercq, P., Rauch, B., Eichler, P., Mikoviny, T. and Wisthaler,
1105 A.: Impact of Alternative Jet Fuels on Engine Exhaust Composition during the 2015 ECLIF
1106 Ground-Based Measurements Campaign, Environ. Sci. Technol., 52(8), 4969–4978,
1107 doi:10.1021/acs.est.7b06244, 2018.

1108 Schripp, T., Herrmann, F., Oßwald, P., Köhler, M., Zschocke, A., Weigelt, D., Mroch, M. and
1109 Werner-Spatz, C.: Particle emissions of two unblended alternative jet fuels in a full scale jet

1110 engine, *Fuel*, 256, 115903, doi:10.1016/j.fuel.2019.115903, 2019.

1111 Snelling, D. R., Smallwood, G. J., Liu, F., Gülder, Ö. L. and Bachalo, W. D.: A calibration-
1112 independent laser-induced incandescence technique for soot measurement by detecting
1113 absolute light intensity, *Appl. Opt.*, 44(31), 6773, doi:10.1364/ao.44.006773, 2005.

1114 Timko, M. T., Yu, Z., Onasch, T. B., Wong, H. W., Miake-Lye, R. C., Beyersdorf, A. J., Anderson,
1115 B. E., Thornhill, K. L., Winstead, E. L., Corporan, E., Dewitt, M. J., Klingshirn, C. D., Wey, C.,
1116 Tacina, K., Liscinsky, D. S., Howard, R. and Bhargava, A.: Particulate emissions of gas
1117 turbine engine combustion of a fischer-tropsch synthetic fuel, *Energy Fuels*, 24(11), 5883–
1118 5896, doi:10.1021/ef100727t, 2010.

1119 Timko, M. T., Fortner, E., Franklin, J., Yu, Z., Wong, H. W., Onasch, T. B., Miake-Lye, R. C. and
1120 Herndon, S. C.: Atmospheric measurements of the physical evolution of aircraft exhaust
1121 plumes, *Environ. Sci. Technol.*, 47(7), 3513–3520, doi:10.1021/es304349c, 2013.

1122 Trueblood, M. B., Lobo, P., Hagen, D. E., Achterberg, S. C., Liu, W. and Whitefield, P. D.:
1123 Application of a hygroscopicity tandem differential mobility analyzer for characterizing
1124 PM emissions in exhaust plumes from an aircraft engine burning conventional and
1125 alternative fuels, *Atmos. Chem. Phys.*, 18(23), doi:10.5194/acp-18-17029-2018, 2018.

1126 Ugarte, D.: Curling and closure of graphitic networks under electron-beam irradiation,
1127 *Nature*, 359(6397), 707–709, doi:10.1038/359707a0, 1992.

1128 Virkkula, A.: Erratum: Calibration of the 3-wavelength particle soot absorption
1129 photometer (3λ PSAP) (*Aerosol Science and Technology* (2002) 39 (68-83)), *Aerosol Sci.*
1130 *Technol.*, 44(8), 706–712, doi:10.1080/02786826.2010.482110, 2010.

1131 Vozka, P., Vrtiška, D., Šimáček, P. and Kilaz, G.: Impact of Alternative Fuel Blending
1132 Components on Fuel Composition and Properties in Blends with Jet A, *Energy Fuels*, 33(4),
1133 3275–3289, doi:10.1021/acs.energyfuels.9b00105, 2019.

1134 Vander Wal, R. L. and Choi, M. Y.: Pulsed laser heating of soot: morphological changes,
1135 *Carbon N. Y.*, 37(2), 231–239, doi:10.1016/S0008-6223(98)00169-9, 1999.

1136 Vander Wal, R. L., Bryg, V. M. and Huang, C.-H.: Aircraft engine particulate matter: Macro-
1137 micro- and nanostructure by HRTEM and chemistry by XPS, *Combust. Flame*, 161(2), 602–
1138 611, doi:10.1016/j.combustflame.2013.09.003, 2014.

1139 Williams, P. I., Allan, J. D., Lobo, P., Coe, H., Christie, S., Wilson, C., Hagen, D., Whitefield, P.,
1140 Raper, D. and Rye, L.: Impact of alternative fuels on emissions characteristics of a gas
1141 turbine engine - Part 2: Volatile and semivolatile particulate matter emissions, *Environ.*
1142 *Sci. Technol.*, 46(19), doi:10.1021/es301899s, 2012.

1143 Wilson, G. R., Edwards, T., Corporan, E. and Freerks, R. L.: Certification of alternative
1144 aviation fuels and blend components, *Energy Fuels*, 27(2), 962–966,
1145 doi:10.1021/ef301888b, 2013.

1146 Yuan, R., Lobo, P., Smallwood, G. J., Johnson, M. P., Parker, M. C., Butcher, D., &
1147 Spencer, A. (2022). Measurement of black carbon emissions from multiple engine
1148 and source types using laser-induced incandescence: sensitivity to laser fluence.
1149 *Atmospheric Measurement Techniques*, 15(2), 241–259. [doi:10.5194/amt-15-241-2022](https://doi.org/10.5194/amt-15-241-2022). 2022.

1151

1152 7 Figures and Tables

1153 Table 1. Properties of the fuels used for the ground-based measurements (fuel
1154 samples acquired from wing-tank after test).

Property	Method	JP-8	REF3	REF4	SAF1	SAF2	SAF3
Aromatics	ASTM	19.9	18.6	16.5	8.5	9.5	15.2
[vol%]	D1319						
Hydrogen H	ASTM	13.86	13.65	14.08	14.40	14.51	14.04
[mass%]	D7171						
Sulphur, total	ISO	1240	105	5.7	56.8	4.1	58.6
[ppm]	20884						
Naphthalenes	ASTM	1.49	1.17	0.13	0.61	0.05	0.64
[mass%]	D1840						
Smoke point	ASTM	23.0	23.0	27.0	30.0	30.0	28.0
[mm]	D1322						

1155

1156 Table 2. Instruments used to measure nvPM and key measured properties. All instruments reported data at 1 second intervals except the
 1157 SMPSs (45 second intervals for NRC and DLR, 60 seconds for NASA) and filter samplers. Instrument abbreviations are defined in the text.

Operator	Instrument	Acronym	Species measured	Sampling duration [s]	Units	Penetration functions ^d
NASA	Particle soot absorption photometer	PSAP	nvPM ^a mass	1	$\mu\text{g m}^{-3}$	1
	Tricolor absorption photometer	TAP	nvPM ^a mass	1	$\mu\text{g m}^{-3}$	1
	Scanning mobility particle sizer	SMPS	Total PSD (10 to 278 nm)	45	particles cm^{-3} , and $\mu\text{g m}^{-3}$	1
	Thermo-denuder with SMPS	TD-SMPS	nvPM PSD ^b (10 to 278 nm)	45	$\mu\text{g m}^{-3}$	1, 4
NRC	CO ₂ sensor	LI-COR 7000	CO ₂	1	ppmv	-
	Cavity-attenuated phase shift PM _{SSA} monitor (660 nm)	CAPS (NRC)	nvPM ^a mass	1	$\mu\text{g m}^{-3}$	1
	Photoacoustic extictiometer	PAX	nvPM ^a mass	1	$\mu\text{g m}^{-3}$	1
	Laser-induced-incandescence	LII 300 (NRC; 2x)	nvPM ^b mass	1	$\mu\text{g m}^{-3}$	1
	Catalytic stripper SMPS	CS-SMPS	nvPM PSD (8.6 to 278 nm)	45	particles cm^{-3}	1, 3
MST (NARS)	AVL Particle Counter Advanced	APC	nvPM number	1	particles cm^{-3}	1, 2
	Micro Soot Sensor	MSS Plus	nvPM ^a mass	1	$\mu\text{g m}^{-3}$	1, 2
	Laser-induced-incandescence	LII-300 (NARS)	nvPM ^c mass	1	$\mu\text{g m}^{-3}$	1, 2
	CO ₂ sensor	LI-COR 840A	CO ₂	1	ppm	-
	Differential mobility spectrometer	DMS500	Total PSD (5 to 1000 nm)	1	particles cm^{-3}	1, 2
ARI	Cavity-attenuated phase shift PM _{SSA} monitor (630 nm)	CAPS (ARI)	nvPM ^a mass	1	$\mu\text{g m}^{-3}$	1, 2

1158 ^anvPM measured via particulate absorption as equivalent BC (eBC). ^bParticle size distribution, here measured with respect to mobility diameter. ^cnvPM measured
 1159 via laser-induced incandescence as refractory BC (rBC). ^dNumbers are indices corresponding to the penetration functions shown in Figure 4.

1160 Table 3. Summary of the ratios between the EI_m of individual instruments and the
 1161 geometric mean of the Group 1 (real time) instruments. The corresponding raw
 1162 data are shown in Figure 11. Regression: linear regression against Group 1
 1163 geometric mean weighted by standard deviations, with $k = 2$ uncertainties from fit.
 1164 SD: standard deviation. RSD: Relative SD. Group 1: real time instruments. Group 2:
 1165 integrative instruments.

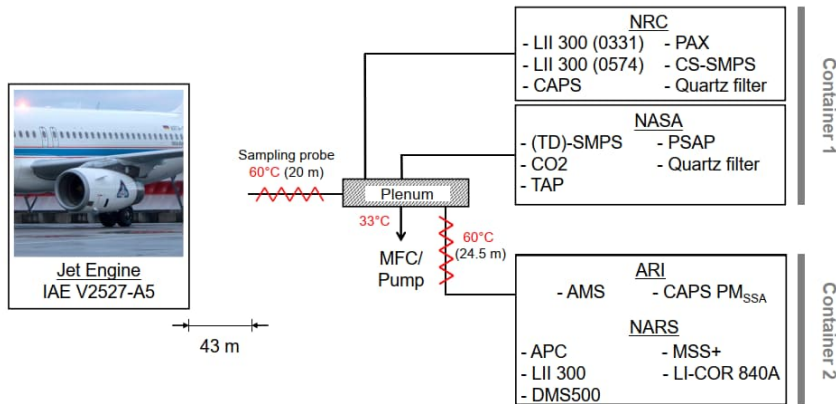
1166

Group	Instrument	EI _{mass} Ratio			Regression	
		vs. Group 1	RSD			vs. Group 1
		Mean	SD	[%]	Intercept	Slope
1	CAPS PM _{SSA} (<i>ARI</i>)	0.84	0.08	10	12 ± 19	0.8 ± 0.1
1	CAPS PM _{SSA} (<i>NRC</i>)	0.99	0.09	9	-0.3 ± 0.8	1.01 ± 0.04
1	LII (<i>NARS</i>)	1.24	0.18	15	27 ± 6	1.03 ± 0.04
1	LII (<i>NRC-0331</i>)	1.07	0.1	9	-15 ± 42	1.17 ± 0.16
1	LII (<i>NRC-0574</i>)	0.78	0.08	10	-17.1 ± 2	0.88 ± 0.08
1	MSS+	1.07	0.14	13	17.8 ± 5	0.92 ± 0.04
1	PAX	1.06	0.18	17	-15 ± 1	1.21 ± 0.02
2	CS-SMPS	1.50	0.27	18	12 ± 22	1.02 ± 0.12
2	TD-SMPS	1.14	0.26	23	-5 ± 1	1.47 ± 0.04
2	PSAP ^a	0.89	0.32	36	8 ± 16	0.82 ± 0.08
2	TAP ^b	0.88	0.12	14	6 ± 6	0.75 ± 0.02

Formatted: Superscript

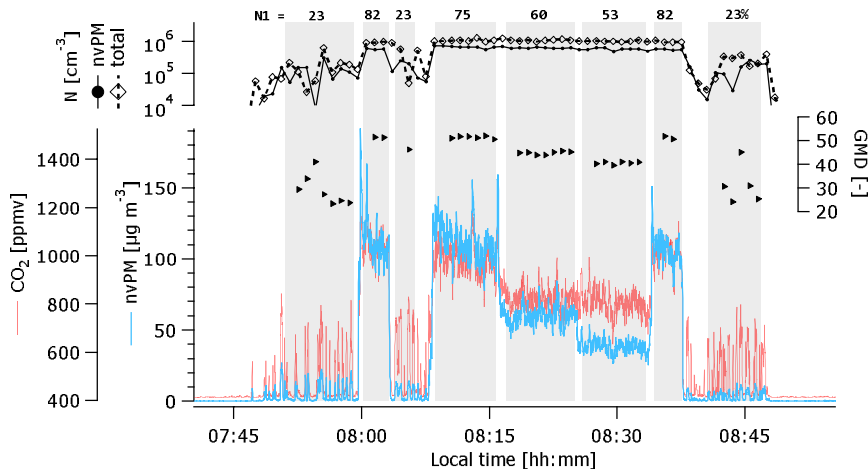
Formatted: Superscript

1167 ^aPSAP operated at 10% of its nominal flow rate. ^bTAP operated at 5% of its
 1168 nominal flow rate.



1169

1170 Figure 1. Schematic of sampling configuration behind the DLR ATRA aircraft. The length
 1171 and flow rate of sampling lines from the manifold to the various instruments varied as
 1172 described in the text. The NRC and NASA instruments were all placed within Container 1,
 1173 while the NARS and ARI instruments were placed in Container 2. For simplicity, the figure
 1174 omits a short heated line connecting the first plenum to the NARS. The ARI instruments
 1175 were downstream of all NARS instruments except the DMS500 (see Lobo et al., 2016 for
 1176 detailed NARS diagram). NARS = North American Reference System.



1177

1178 Figure 2. Illustration of a typical test run. Variation in the CO₂ concentration was not due
 1179 to instrument noise, as illustrated by the CO₂ measurements prior to and following
 1180 sampling. A representative nvPM mass instrument is shown by the blue trace. Sizing
 1181 information (GMD) is shown by the black symbols (triangles: GMD; diamonds with dashed
 1182 line: total PM number; spheres with solid line: nvPM number measured with the CS-
 1183 SMPS).

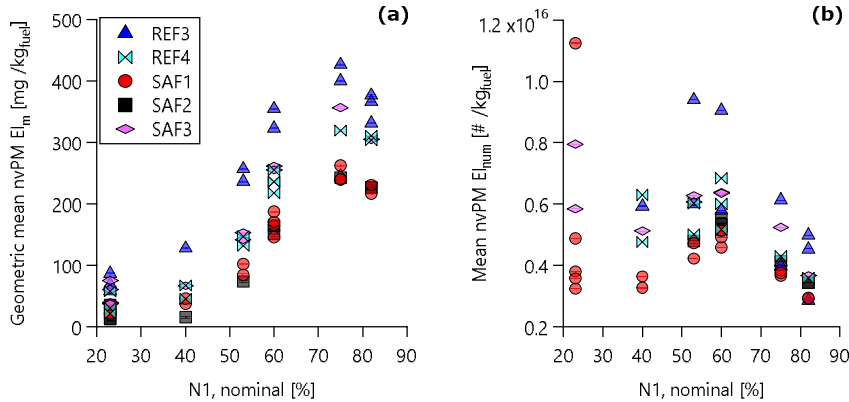


Figure 3. Relationship between nvPM (a) EI_m and (b) EI_{num} with $N1$ for all data obtained with the V2527-A5 engine. The trends shown in this plot are discussed further in the companion article (Schripp et al., 2022). The ordinate values are the geometric mean discussed in the text.

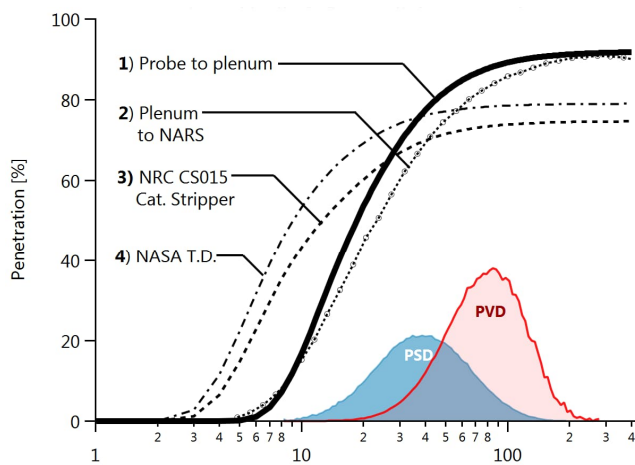
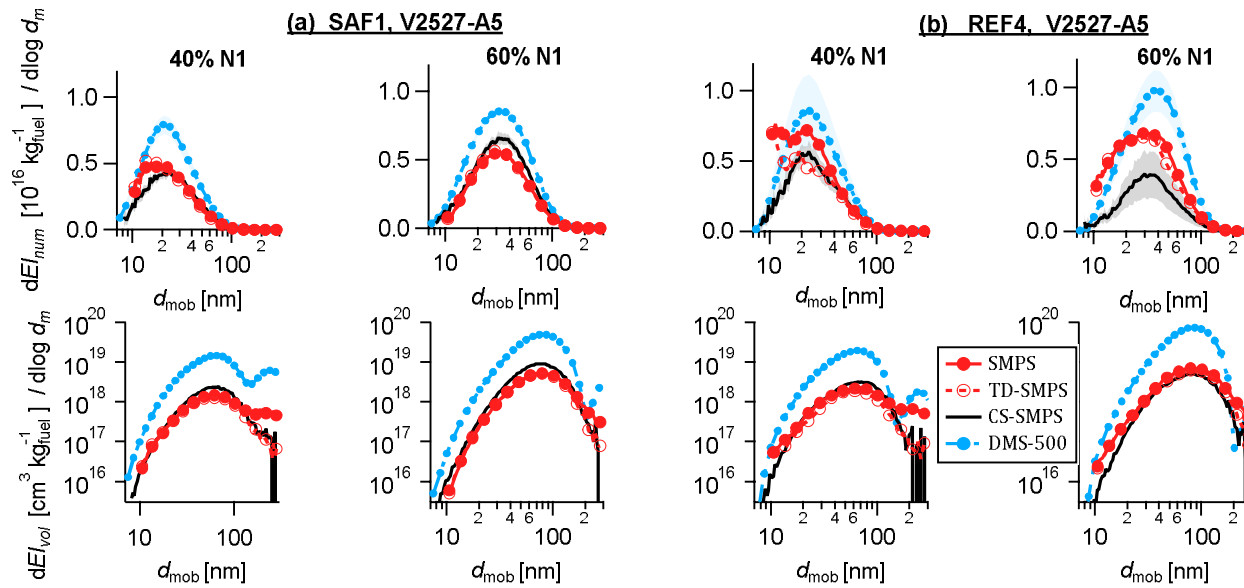


Figure 4. Penetration functions for the main probe-to-plenum sampling line as well as other components in the sampling system. Shaded areas illustrate a representative particle size (PSD) and volume (PVD) distribution measurement with GMD 34 nm and GSD 1.72. PSD data for all test points and instruments are provided in the [Data Availability section](#). NARS: North American Reference System; CS015: Catalytic Stripper; T.D.: thermodenunder.

Deleted: supplement



1200 Figure 5. Selected PSDs illustrating the V2527-A5 engine with (a) SAF1 fuel and (b) REF4 fuel. Each panel shows 60% N1 on the right and a lower N1
 1201 on the left: 40% for (a), 60% for (b). Note that the TD-SMPS and CS-SMPS (red open circles and black line) represent nvPM, while the SMPS and
 1202 DMS500 represent vPM.
 1203

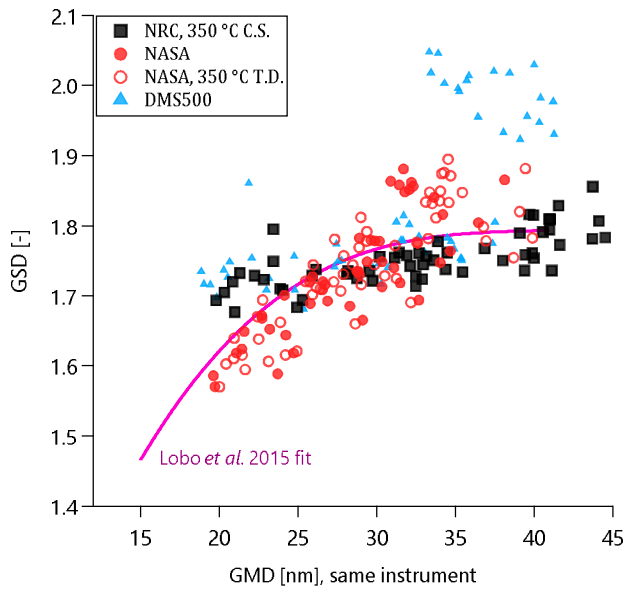
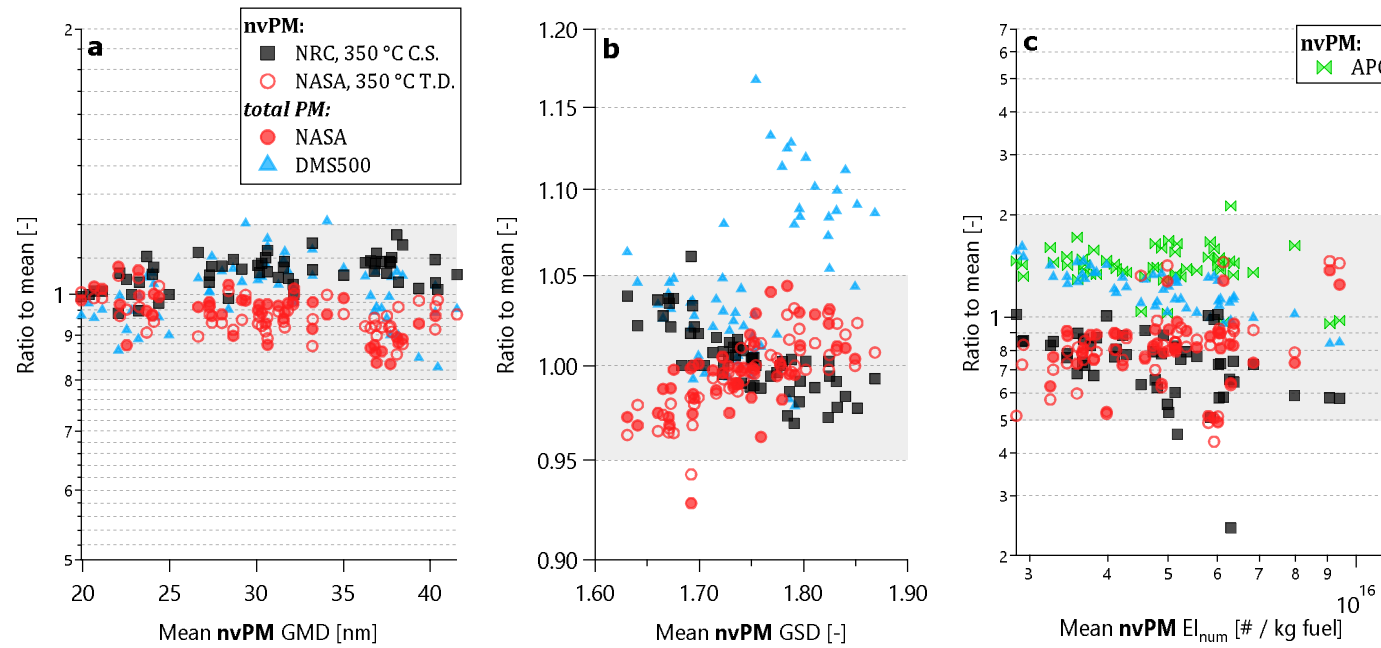


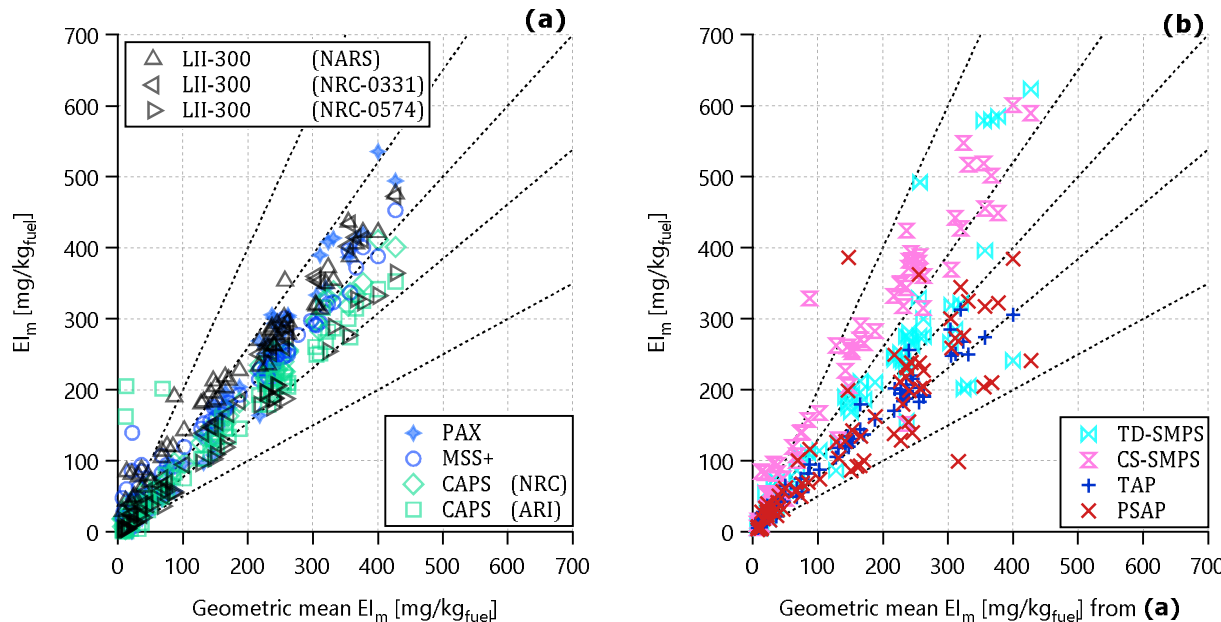
Figure 6. GSD versus GMD data as by measured by each particle sizer for all test points. Higher GSDs for the DMS500 correspond to bimodal PSDs (non-volatile and volatile modes). Note that size-dependent particle losses (see penetration functions in Figure 4) may affect both GSD and GMD. Based on Figure 12, the TD-SMPS (NASA) data may be more accurate than the CS-SMPS data (see text). Fit is from Lobo et al. (2015c).



1210

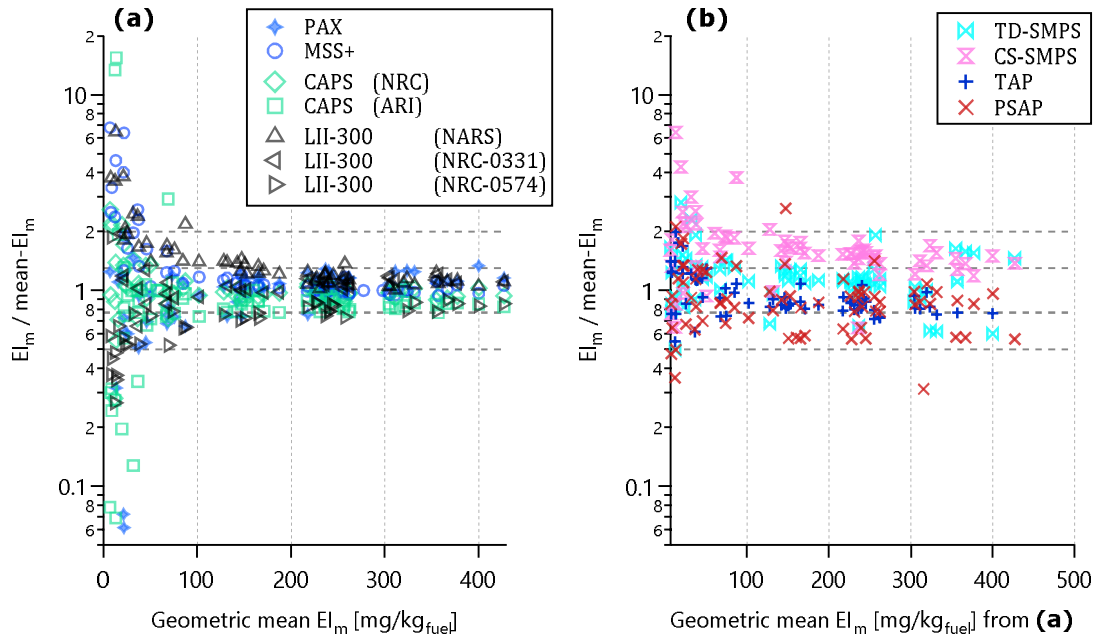
1211 Figure 7. Comparison of size and number measurements in terms of GMD, GSD, and EI_n . Grey shading shows 20%, 5%, and 200% in GMD, GSD, and
 1212 EI_n , respectively. In panels (a) and (b), mean is defined from the CS-SMPS (NRC) and TD-SMPS (NASA) data. In panel (c), the mean additionally
 1213 includes the APC (NARS) data (the APC is in the NARS and uses a TSI 3790E CPC).

1214



1215

1216 Figure 8. EI_m scatterplot for (a) real-time and (b) integrative nvPM measurements. The term integrative refers to SMPS measurements (mass
 1217 concentrations estimated by assuming unit-density spheres) and filter photometer measurements (mass concentrations estimated using standard
 1218 empirical relationships between light attenuation and light absorption). The abscissa of both panels is the geometric mean of all available data from
 1219 the 7 real-time sampling instruments plotted in (a). Angled lines illustrate slopes of 2, 2⁻¹, 1.3, 1.3⁻¹, and 1.0.



1220

1221

1222

1223

Figure 9. Ratio plots corresponding to Figure 8. The inner and outer horizontal lines show ratios of 2, 2⁻¹, 1.3, 1.3⁻¹, and 1.0. Agreement between the instruments is poorer at $EI_m < 100$ mg/kg_{fuel}, which corresponds to an approximate concentration of 10 $\mu\text{g m}^{-3}$ (the exact conversion factor varies with CO_2 concentration and fuel properties) and close to the limit of detection for most instruments.

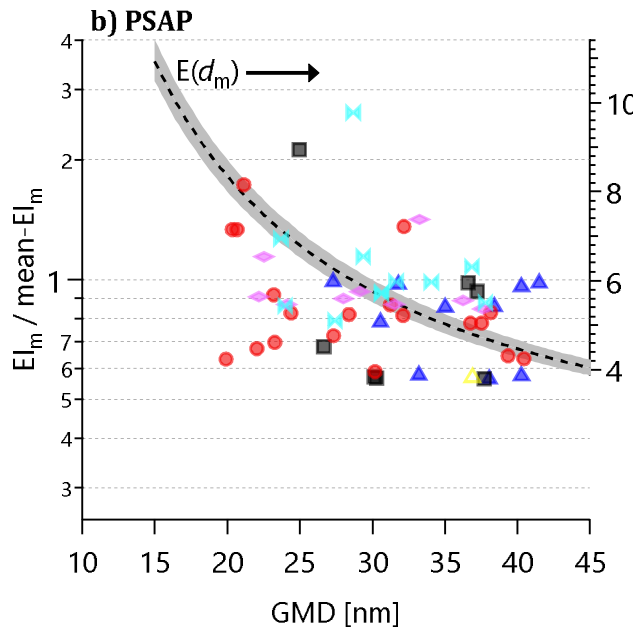
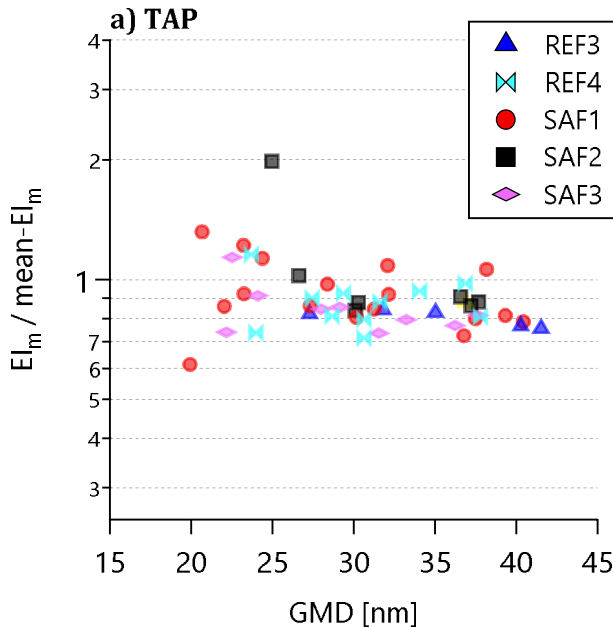
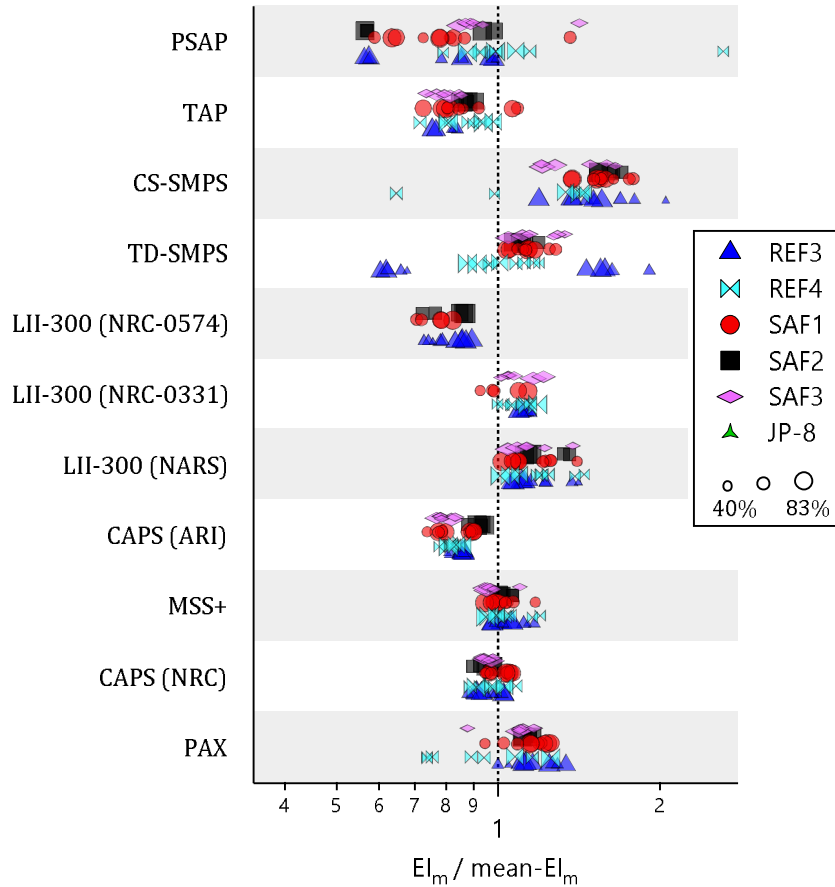
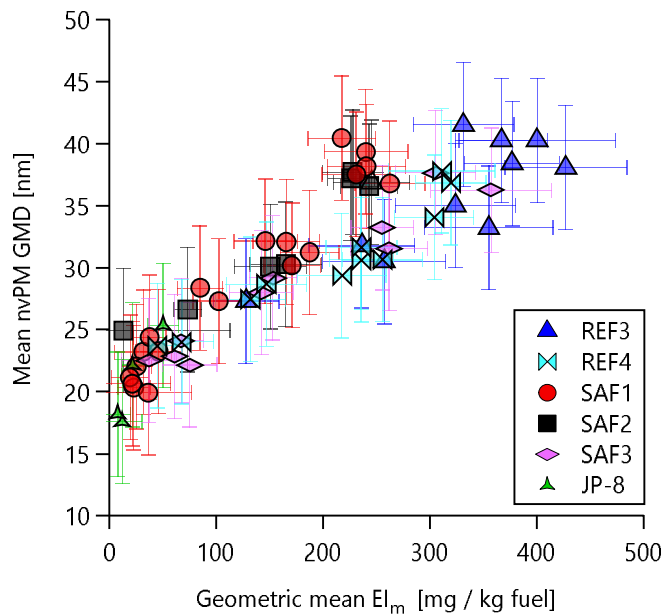


Figure 10. $EI_m / \text{mean-}EI_m$ ratios from Figure 9 for the TAP and PSAP (the filter-based photometers) only, plotted as a function of geometric mean mobility diameter (GMD) to highlight potential size-dependent sensitivities of these instruments. The curve labelled $E(d_m)$ in b) plots the size-dependent PSAP correction factor given by Nakayama et al. (2010; Eq. 8) with 1σ uncertainties shaded. Note that the TAP and PSAP were operated at 5% and 10% of their nominal flow rates, respectively, for all measurements in this study.

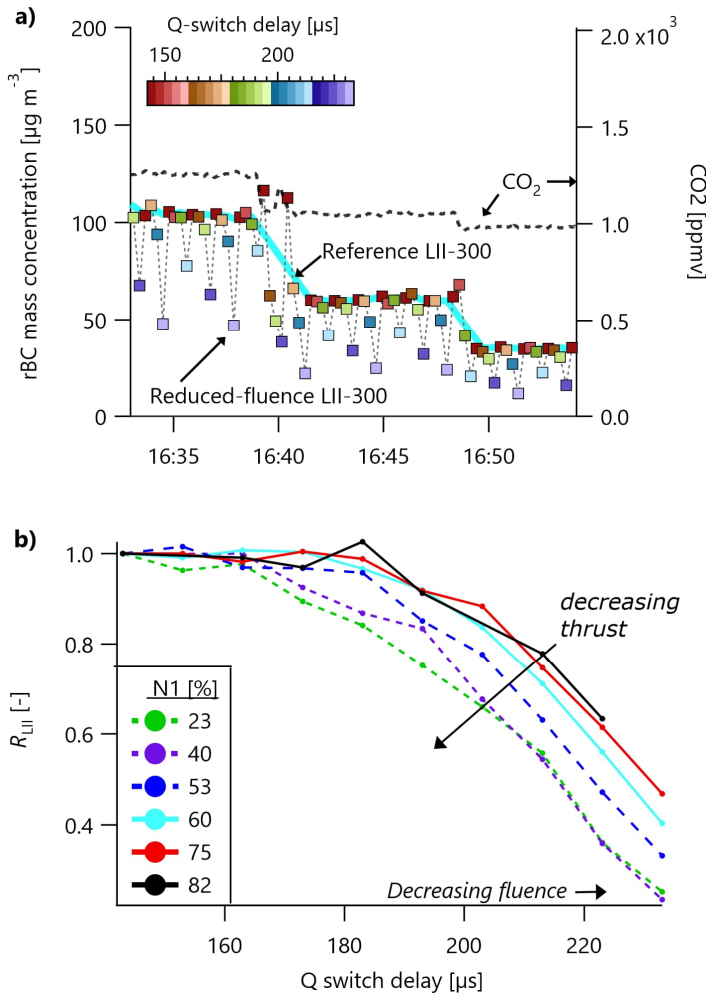


1229

1230 Figure 11. Ratios of Figure 9 grouped by fuel. All fuels except JP-8 were combusted in the
 1231 V2527-A5 engine; JP-8 was combusted in the CFM56-2C1 engine. Shading is to guide the
 1232 eye. Symbols are sized by N1 thrust. Plot excludes data where $EI_m < 25 \text{ mg/kg}_{\text{fuel}}$ and N1
 1233 thrust below 40% to minimize the effects of instrument noise and wind speed,
 1234 respectively, on the ratios.



1235
1236 Figure 12. Scatterplot of the mean nvPM GMD within test points against geometric
1237 mean nvPM EI_m from Figure 8a. The correlation with GMD and EI_m indicates that Figure 9
1238 implicitly represented different particle sizes.



1241
1242 Figure 13. (a) LII 300 experiment time series, where one LII 300 was operated with
1243 increased Q-switch delays to reduce its laser fluence (squares) and the other was operated
1244 at standard fluence (solid line). CO_2 data are also shown for context. (b) The ratio R_{LII} of
1245 the concentration reported by the reduced-fluence LII divided by the reference LII. It is
1246 evident from (b) that the standard high-fluence conditions generate data that are
1247 independent of N1 thrust, and that moderate- and low-fluence conditions (Q-switch delays
1248 greater than about 165 to 185 μs) display a weak dependence on thrust.

1249